

The 26 December 2001 Solar Eruptive Event Responsible for GLE63. III. CME, Shock Waves, and Energetic Particles

V.V. Grechnev¹ · V.I. Kiselev¹ ·
A.M. Uralov¹ · K.-L. Klein² ·
A.A. Kochanov¹

Received ; accepted

© Springer ●●●

Abstract The SOL2001-12-26 moderate solar eruptive event (GOES importance M7.1, microwaves up to 4000 sfu at 9.4 GHz, CME speed 1446 km s^{-1}) produced strong fluxes of solar energetic particles and ground-level enhancement of cosmic-ray intensity (GLE63). To find a possible reason for the atypically high proton outcome of this event, we study multi-wavelength images and dynamic radio spectra and quantitatively reconcile the findings with each other. An additional eruption probably occurred in the same active region about half an hour before the main eruption. The latter produced two blast-wave-like shocks during the impulsive phase. The two shock waves eventually merged around the radial direction into a single shock traced up to $25 R_{\odot}$ as a halo ahead of the expanding CME body, in agreement with an interplanetary Type II event recorded by the *Radio and Plasma Wave Investigation* (WAVES) experiment on the *Wind* spacecraft. The shape and kinematics of the halo indicate an intermediate regime of the shock between the blast wave and bow shock at these distances. The results show that i) the shock wave appeared during the flare rise and could accelerate particles earlier than usually assumed; ii) the particle event could be amplified by the preceding eruption, which stretched closed structures above the developing CME, facilitated its lift-off and escape of flare-accelerated particles, enabled a higher CME speed and stronger shock ahead; iii) escape of flare-accelerated particles could be additionally facilitated by reconnection of the flux rope, where they were trapped, with a large coronal hole; iv) the first eruption supplied a rich seed population accelerated by a trailing shock wave.

¹ Institute of Solar-Terrestrial Physics SB RAS, Lermontov St. 126A, Irkutsk 664033, Russia; email: grechnev@iszf.irk.ru
email: valentin.kiselev@iszf.irk.ru email: uralov@iszf.irk.ru
email: kochanov@iszf.irk.ru

² LESIA-UMR 8109, Observatoire de Paris, CNRS, Univ. Paris 6 & 7, Observatoire de Meudon, F-92195 Meudon, France; email: ludwig.klein@obspm.fr

Keywords: Coronal Mass Ejections; Cosmic Rays, Solar; Energetic Particles; Flares; Radio Bursts; Waves, Shock

1. Introduction

Solar energetic particles (SEP), which are accelerated in association with solar eruptive events, pose a hazard for equipment and astronauts on spacecraft, and even for crew members and passengers on aircraft in high-latitude flights because of secondary particles produced in the Earth's atmosphere. SEPs mainly consist of protons, α -particles, and heavier ions. Their energies reach hundreds of MeV and sometimes up to several GeV. The highest-energy extremity of SEPs occasionally produces considerable fluxes of secondary neutrons observed as ground-level enhancements (GLE) of cosmic-ray intensity. Seventy-two GLEs have been registered since 1942 up to the present time, mainly with high-latitude neutron monitors (see, *e.g.*, Cliver, 2006; Belov *et al.*, 2010; Nitta *et al.*, 2012; Miroshnichenko, Vashenyuk, and Pérez-Peraza, 2013 and references therein). On average, GLEs occur once a year, but very irregularly. GLEs avoid solar minima, while four GLEs occurred within one week in May 1990. The rareness of GLEs hampers understanding their origins and emphasizes the importance of studying each solar event responsible for a GLE.

One presumable source of SEPs and GLEs is traditionally associated with flare processes in coronal magnetic fields of active regions exhibited in X-ray and microwave emissions. Another probable source of SEPs is related to bow shocks driven by fast coronal mass ejections (CMEs). In spite of the high practical importance of SEP events, consensus has not been reached so far about the probable contributions from the two sources in different events and energy ranges. The main subject of the debates is related to the origins of high-energy SEPs and especially GLEs (see, *e.g.*, Klein and Trottet, 2001; Kallenrode, 2003; Grechnev *et al.*, 2008a; Reames, 2009a; Aschwanden, 2012; Miroshnichenko, Vashenyuk, and Pérez-Peraza, 2013 for a review and references). Each competing concept is supported by convincing arguments (Tylka *et al.*, 2005; Chupp and Ryan, 2009; Vilmer, MacKinnon, and Hurford, 2011; Rouillard *et al.*, 2012; Reames, 2013).

The traditional view on the SEP origins is mainly based on the hypotheses proposed in the past decades, when observational opportunities were strongly limited relative to modern ones. Traditional concepts considered the processes responsible for acceleration of particles in flares and those by shock waves to be remote and completely independent of each other. Observational studies of the two last decades update the view on solar eruptive phenomena step by step and establish their close association with each other.

Zhang *et al.* (2001) and Temmer *et al.* (2008, 2010) found synchronization between the CME acceleration pulse and hard X-ray (HXR) and microwave bursts. Qiu *et al.* (2007) established that the helical component of the CME's flux rope (responsible for its acceleration) is formed by reconnection, which caused a flare. Miklenic, Veronig, and Vršnak (2009) found a quantitative correspondence between the reconnected magnetic flux and the rate of flare energy release. Grechnev *et al.* (2011, 2013a, 2015b, 2016) established that waves were

impulsively excited by erupting flux ropes inside developing CMEs during the rise phase of HXR and microwave bursts and rapidly steepened into the shocks because of a rapid falloff of the fast-mode speed. Then the shock wave quasi-freely propagates for some time like a decelerating blast wave and changes to the bow-shock regime later, if the trailing CME is fast.

These results and the outlined scenario show that the traditional contrasting of the acceleration in a flare and by a shock might be exaggerated. Two consequences are important for the SEP acceleration issue. First, shock waves appear much earlier than previously assumed and can accelerate heavy particles even during the flare. Second, a close association is expected between the parameters of the CME, shock wave, and flare, on the one hand, and those of a SEP event.

These circumstances indicate that both flare-related and shock-related acceleration can be significant in SEP production, while their roles might depend on particular conditions in different events. Recent studies by Dierckxens *et al.* (2015); Trotter *et al.* (2015); Grechnev *et al.* (2015a) confirmed this idea and indicated statistically increasing importance of the flare-related particle acceleration at higher energies. The shock-related contribution was also manifest.

In Article I (Grechnev and Kochanov, 2016) and Article II (Grechnev *et al.*, 2017) we started analyzing the SOL2001-12-26 event related to an M7.1 flare with a peak time at 05:40 (all times hereafter refer to UTC if not specified otherwise) responsible for GLE63. Among all GLE-related flares of Solar Cycle 23, this flare had the lowest GOES importance and longest duration, being associated with a moderate microwave burst. Limited observations of the flare and eruption determined incomplete knowledge of this solar event. No soft X-ray (SXR) images or HXR data are available. Observations with the *Extreme-ultraviolet Imaging Telescope* (EIT: Delaboudinière *et al.*, 1995), onboard the *Solar and Heliospheric Observatory* (SOHO), had a gap from 04:47 to 05:22.

Some aspects of this event look challenging. If protons and heavier ions were accelerated in the flare concurrently with electrons, then it is not clear why the SEP fluxes were so large. If they were shock-accelerated, then it is not clear why the fast CME and strong shock developed in association with a moderate flare. It is also not clear when and where the shock wave appeared and how it evolved.

Articles I and II analyzed the event from microwave imaging observations with the *Siberian Solar Radio Telescope* (SSRT: Smolkov *et al.*, 1986; Grechnev *et al.*, 2003) at 5.7 GHz; the *Nobeyama Radioheliograph* (NoRH; Nakajima *et al.*, 1994) at 17 and 34 GHz and total flux data of *Nobeyama Radio Polarimeters* (NoRP: Nakajima *et al.*, 1985), and the ultraviolet (UV) images from the *Transition Region and Coronal Explorer* (TRACE: Handy *et al.*, 1999) in 1600 Å.

The results of Articles I and II related to the particle event are as follows.

- i) GLE63 was most likely caused by the M7.1 event in Active Region (AR) 9742 (N08 W54). Implication of a hypothetical concurrent far-side event is unlikely.
- ii) The flare was much longer than other GLE-related flares and consisted of two parts, each of which was most likely caused by a separate eruption.
- iii) The first eruption presumably occurred in AR 9742 around 04:40 and produced ejecta. They were not observed. A related moderate two-ribbon flare involved medium magnetic fields and reached a GOES importance of M1.6.

- iv) The second eruption occurred in AR 9742 around 05:04 and produced a fast CME. The related main two-ribbon flare involved strong magnetic fields associated with a sunspot and reached an importance of M7.1.
- v) An additional sharp jet-like eruption around 05:09 may have produced a shock wave.

Based on these results, in this article we analyze the eruptions in this event from indirect observations. We endeavor to reconstruct the CME and shock wave, their evolution, and to find which circumstances could amplify the SEP outcome of this event. Pursuing the last issue, we compare the 26 December 2001 event with other SEP and GLE events. Invoking the recent observational conclusions about scenarios of the CME and shock-wave development listed in this section, we revisit this historical GLE-related event on the basis of the modern view.

Section 2 continues the introduction and presents an overview of the main features of the SEP event. Section 3 outlines the flare and reveals the eruptions. Analyzing drifting radio bursts in a wide frequency range, Section 4 reconstructs the eruptive event, reveals the shock waves, and addresses a long-standing issue of the relation between metric and interplanetary Type II events. Section 5 considers the CME. Section 6 discusses the results, evolution of the CME and shock wave, indications of particle release, and the possible causes of the enhanced SEP outcome of this event. Section 7 summarizes the conclusions of the study.

2. Overview of the Particle Event

This section outlines the 26 December 2001 SEP event, whose possible sources are in question. We list its main properties found by different authors and comment on their conclusions. We compare the 26 December 2001 event with other SEP and GLE events to find their similarity, possible differences, and hints at the probable causes of its enhanced SEP outcome. The arguments in favor of each competing concept of the SEP origin are listed. More information can be found in the references cited.

2.1. Near-Earth Proton Enhancement

SEPs are dominated by accelerated protons. Figure 1 presents two-day time-profiles of the SXR flux from the flare and the proton flux in three standard integral channels of GOES-8. Figure 1b additionally shows the flux of high-energy protons > 700 MeV recorded by the *High-Energy Proton and Alpha Detector* (HEPAD) on GOES-8 magnified by a factor of 100.

The pre-event background does not show any elevated seed population, as was the case before GLE33 and GLE35 addressed by Cliver (2006), and his conclusion about these events does not provide a straightforward key to understanding GLE63. The time-profiles of the proton fluxes are typical of well-connected events, with a sharp rise roughly corresponding to the flare peak followed by a moderately long decay. HEPAD detected a highest-energy > 700 MeV enhancement, which is usual in GLE events. Each integral channel is dominated by protons in its lowest-energy part because of their declining spectrum. The

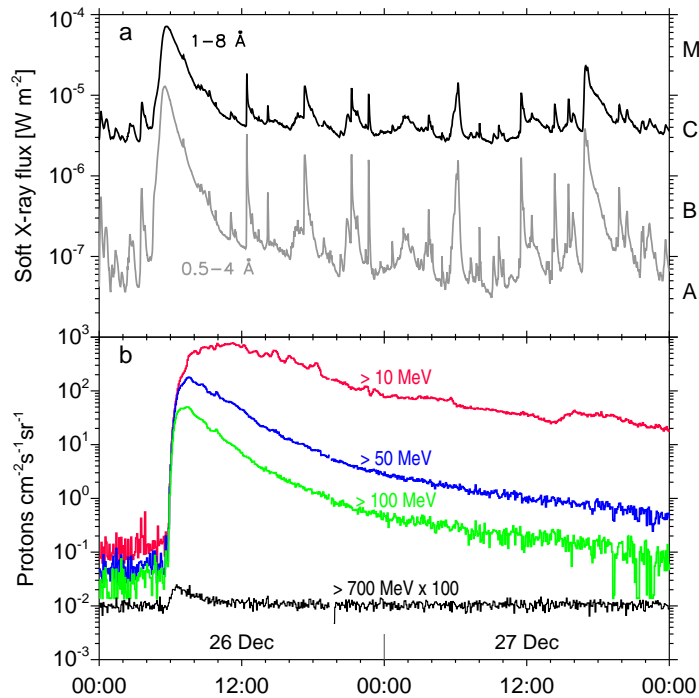


Figure 1. Time profiles of the soft X-ray flux (a) and near-Earth proton enhancement (b) recorded by three standard integral channels of GOES-8 and the high-energy HEPAD detector (> 700 MeV: black, magnified by a factor of 100).

time profiles reflect the energy spectrum of protons, while the path lengths for different energies might not be identical. The increasing duration of the lower-energy proton fluxes is mainly caused by their transport in the interplanetary space, primarily the velocity dispersion. It is not possible to exclude contributions from two different accelerators, one of which operated longer, dominating at lower energies, while another of a shorter duration dominated at higher energies.

From an analysis of 35 GLEs (without GLE63) Miroshnichenko, Vashenyuk, and Pérez-Peraza (2013) found the presence of a prompt component with an exponential flux spectrum and a slow power-law component with an average $\langle \gamma \rangle = 4.85 \pm 0.25$. The authors considered this fact incompatible with exclusive acceleration of protons by shock waves, expecting a power-law flux spectrum with $\gamma \approx 2.5$ in this case.

Mewaldt *et al.* (2012) presented the energy spectra of proton fluences and other SEP properties during the 16 GLEs of Solar Cycle 23. The spectra in a range of $\approx 0.1 - 600$ MeV are best fit with double power-laws. On average, the spectra above ≈ 40 MeV in GLE events have a slope of -3.18 with $\sigma = 0.83$, significantly harder than in typical large SEP events (-4.34 , $\sigma = 0.77$). The spectral slopes below the break-energies are similar, being about -1.25 on average. The spectrum of the proton fluence in our event had a slope of -1.53 below 32 MeV and -3.14 at higher energies, close to the average values for other GLEs. The double power-law spectrum seems to favor the dominance of shock-

acceleration at lower energies and flare-acceleration at higher energies advocated by Miroshnichenko, Vashenyuk, and Pérez-Peraza (2013). On the other hand, a double-power-law can result from a single power-law spectrum affected by proton-amplified Alfvén waves near the Sun (see Mewaldt *et al.*, 2012 for a review) or from the acceleration by a quasi-perpendicular shock (Tylka and Lee, 2006).

To summarize, the properties of the 26 December 2001 proton enhancement were typical of well-connected GLE events. There are indications of the contributions from both flare-related and shock-related sources. However, they can also be interpreted in terms of a single shock-wave accelerator, being therefore inconclusive.

2.2. Some Properties of Heavier Ions

The SEP events have traditionally been categorized as gradual or impulsive events (mixed events are also considered). Gradual SEP events are characterized as long-duration, large, intense events. They have average ion abundances similar to those of the corona or solar wind. In contrast, impulsive SEP events are small, have relatively short durations, can have 1000-fold enhancements in ${}^3\text{He}/{}^4\text{He}$ and in heavy elements ($Z > 50$)/O relative to the corona or solar wind, and are associated with solar flares or jets and Type III radio bursts (Reames, 2013). The 26 December 2001 event had a long duration and low ${}^3\text{He}/{}^4\text{He}$ ratio like gradual events (Desai *et al.*, 2006) and exhibited some properties of impulsive events.

Mewaldt *et al.* (2012) examined the Fe/O ratio, which is considered as a diagnostic of flare material. The Fe/O ratio typical of impulsive SEPs is about unity, while that of gradual SEPs is around 0.1. A criterion for Fe-rich GLE events is $\text{Fe}/\text{O} \geq 0.268$ (Tylka *et al.*, 2005). The authors of both studies noted that the Fe-rich GLEs, on average, have much smaller > 30 MeV proton fluences than the Fe-poor GLEs. In our event, the Fe/O ratio in the range 45 to 80 MeV/nucleon was 0.671, and the > 30 MeV proton fluence was 1.16×10^7 protons cm^{-2} , while the latter parameter for the 16 GLEs was in the range $(8.02 \times 10^6 - 4.31 \times 10^9)$ protons cm^{-2} with a logarithmic average of 1.77×10^8 protons cm^{-2} .

At the rise phase of some gradual events, Fe/O is ≈ 1 and diminishes afterwards, suggesting a flare-related prompt component and shock-related slow component. The 26 December 2001 SEP event also showed this behavior. On the other hand, Tylka *et al.* (2013) argued the initial Fe/O enhancement in this event to be a transport effect, advocating only the shock-related accelerator. We note, however, that if really so, then the mentioned pattern established by Tylka *et al.* (2005) and Mewaldt *et al.* (2012) between the event-integrated values of the Fe/O ratio and the > 30 MeV proton fluence did not hold in this event. Thus, invoking the Fe/O ratio still has not determined the source of SEPs on 26 December 2001.

A promising characteristic of the equilibrium temperature in the acceleration region is the mean ionic charge state of iron [$\langle Q_{\text{Fe}} \rangle$]. In 10 out of the 16 GLEs, in which it was measured, $\langle Q_{\text{Fe}} \rangle$ ranged from 11.7 to 22.1. In our event, $\langle Q_{\text{Fe}} \rangle = 20.7$ corresponds to about 10 MK, which seems to indicate flare material. Mewaldt

et al. (2012) point out that the highly ionized > 20 MeV/nucleon ions in this event and some others could also be the result of electron stripping during the acceleration and/or transport process in a sufficiently dense ambient plasma. The authors concerned with this effect consider that, in terms of the traditional concept (*e.g.* Reames, 2009a, 2013), a CME-driven bow-shock can appear and start accelerating ions between ≈ 140 and ≈ 400 Mm above the photosphere. However, recent results listed in Section 1 show that shock-acceleration can occur in still lower corona, and it looks surprising to us in this case that electron stripping is not common, so that high $\langle Q_{\text{Fe}} \rangle \approx 20$ are not always observed.

Thus, the studies of low to moderate-energy protons and heavier ions reveal indications of both shock-related and flare-related contributions in the 26 December 2001 event. However, the latter are not certain and can be interpreted in different ways. Note that the results of these studies were interpreted in terms of old hypotheses, while their update might lead to different conclusions.

2.3. Highest-Energy Particles

The highest-energy manifestations of SEPs on 26 December 2001 are shown in Figure 2. A proxy of ground-level events is presented by the HEPAD proton channel > 700 MeV in Figure 2a. It does not always correspond to a GLE produced by particles of still higher energies $\gtrsim 1$ GeV (Miroshnichenko, Vashenyuk, and Pérez-Peraza, 2013). Figure 2b shows GLE63 recorded by the Apatity and Oulu neutron monitors. The vertical-dashed line denotes the solar particle release time (SPR), 05:20.6 ST ± 3.7 minutes (Solar Time refers to an event on the Sun, leading UTC by the propagation time of light, *i.e.* 05:29:00 UTC ± 3.7 minutes), estimated by Reames (2009b) from the velocity–dispersion analysis (VDA).

A possible indication of heavy ions accelerated to very high energies in our event is presented by preliminary data from the *Trans-Iron Galactic Element Recorder* (TIGER: Geier *et al.*, 2003). TIGER was launched on 21 December 2001 and flew for about 32 days on a long-duration balloon mission from McMurdo Base in Antarctica. Being designed mainly to measure the elemental abundances of galactic cosmic ray nuclei, TIGER observed the 26 December 2001 GLE event in the \approx GeV/nucleon range. Figure 2c shows raw counts produced by heavy elements with $Z > 12$ passing through raw triggers of the device. The shape of the raw TIGER flux is similar to that measured by neutron monitors in Figure 2b, manifesting a common origin of the detected events. No similar deviations from the data gathered during the other time intervals of the flight were observed. Figure 2d shows the ratios of heavy elements that reached the C0 TIGER Cherenkov detector. An interesting point here is that the estimated lower-energy limit of particles that can trigger the C0 detector is around 2.5 GeV/nucleon. During the event, the efficiency of the TIGER track-reconstruction software dropped from $\approx 80\%$ to under $\approx 60\%$, resulting in an additional dead time, that might affect the measured ratio (Geier *et al.*, 2003). Still Figure 2d shows more iron and presents unique evidence that heavy ions could be accelerated to such high energies during this event.

Acceleration of protons and heavier ions in the 26 December 2001 event up to relativistic energies is certain, but their sources still remain unclear. An addi-

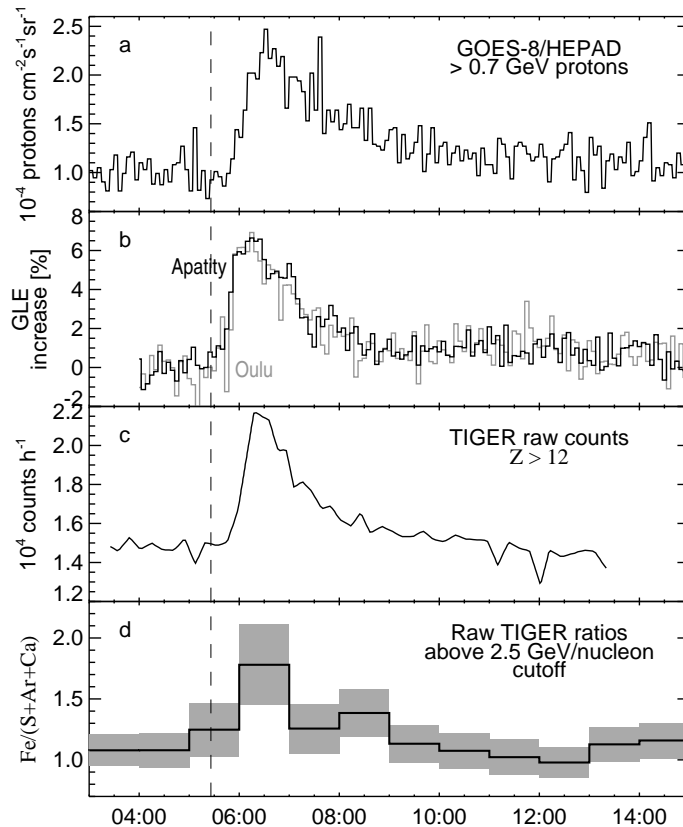


Figure 2. Data on high-energy heavy particles. (a) GOES-8/HEPAD P11 proton channel > 700 MeV. (b) GLE recorded with the Apatity (black) and Oulu (gray) neutron monitors. (c) Raw record of the Antarctic TIGER balloon experiment of response to high-energy ions with $Z \geq 13$. (d) Raw ratios of heavy ions above the 2.5 GeV/nucleon cutoff calculated from the TIGER data. The vertical-dashed line denotes the particle release time (Reames, 2009b).

tional indication can be found from statistical relations between the parameters of SEPs, on the one hand, and those of flares and CMEs, on the other hand.

2.4. Protons vs. 35 GHz Burst and CME Statistics

A correlation between near-Earth proton enhancements and microwave bursts has been known for a long time (Croom, 1971; Castelli and Barron, 1977; Akinian *et al.*, 1978; Melnikov *et al.*, 1991). Kahler (1982) explained this correlation by the “big flare syndrome” (BFS), *i.e.*, a general correspondence between the energy release in an eruptive flare and its various manifestations. According to his idea, SEPs are accelerated by shock waves, while different parameters of eruptive events should correlate with each other, independent of any physical connection between them. Supporting this concept, Kahler (1982) analyzed the correlations between the peak proton fluxes at 20–40 MeV and 40–80 MeV in 50 SEP events observed in 1973–1979, on the one hand, and microwave data

at 8.8 GHz, 15.4 GHz, and two lower frequencies, on the other hand, using the lists of selected parameters. No proxy of any shock parameters was available. Kahler (1982) found that the peak proton fluxes correlated with microwaves no more than with the thermal SXR flare emission. Assuming that protons are accelerated either by flares or by shocks and not by both, he favored shock-acceleration. This conclusion caused skepticism to the correlations between the parameters of SEPs and microwave bursts.

Studies by Grechnev *et al.* (2013b, 2015a) call for rethinking the role of the BFS. They analyzed the relations between the parameters of strong microwave bursts > 1000 sfu ($1 \text{ sfu} = 10^{-22} \text{ W m}^{-2} \text{ Hz}^{-1}$) at 35 GHz observed by NoRP in 1991–2012 and near-Earth proton enhancements > 100 MeV, both from detailed temporal histories. Gyrosynchrotron emission of high-energy electrons depends on their parameters, magnetic field in the source, and its dimensions. These dependencies are different at frequencies below the turnover frequency of the gyrosynchrotron spectrum and above it. The turnover frequency also depends on the parameters listed. Single-frequency data are therefore ambiguous, being below the turnover frequency in one event and above it in another. To minimize this ambiguity, a highest frequency of 35 GHz was chosen, at which stable regular observations are available.

In addition to the proton events related to strong microwave bursts, some big SEPs might have occurred after weaker bursts. A few additional proton enhancements > 100 MeV with peak fluxes $J_{100} > 10$ pfu ($1 \text{ pfu} = 1 \text{ particle cm}^{-2} \text{ s}^{-1} \text{ sr}^{-1}$) were found, whose solar source events occurred within the observational daytime in Nobeyama.

Out of the total set of events, 28 proton enhancements in 1996–2012 were selected, whose sources were not occulted and for which data on the corresponding CMEs are listed in the online CME catalog (cdaw.gsfc.nasa.gov/CMElist/; Yashiro *et al.*, 2004) based on the observations by the SOHO’s *Large Angle and Spectroscopic Coronagraph* (LASCO; Brueckner *et al.*, 1995). Because the speeds listed in the CME catalog are measured for the fastest feature, V_{CME} for fast CMEs are most likely related to shock waves (Ciaravella, Raymond, and Kahler, 2006). The halo shock fronts ahead of fast CMEs should have the shapes close to spheroidal ones (Grechnev *et al.*, 2011, 2013a, 2014b; Kwon, Zhang, and Olmedo, 2014; Kwon, Zhang, and Vourlidas, 2015); thus, the plane-of-the sky speeds measured in the catalog should not be much different from the modules of their vectors (“space speeds”), especially in the logarithmic scale.

Figure 3 supplements the results of the analysis by Grechnev *et al.* (2015a). Figure 3a shows the scatter plot of the peak proton flux, J_{100} , *vs.* peak microwave flux, F_{35} . The open squares and black triangle (our event) represent the SEPs with $J_{100} > 10$ pfu related to the bursts with $F_{35} \leq 1000$ sfu. These five points are displaced from the majority of SEPs denoted by the filled-gray circles, which show a trend between F_{35} and J_{100} with a Pearson correlation coefficient of 0.75. This figure is analogous to what Kahler (1982) presented for lower proton energies and shows a similar result. For the whole set of events, the correlation coefficient between V_{CME} and J_{100} in Figure 3b is higher, and the five proton-abundant events fall mostly within the main cloud of points.

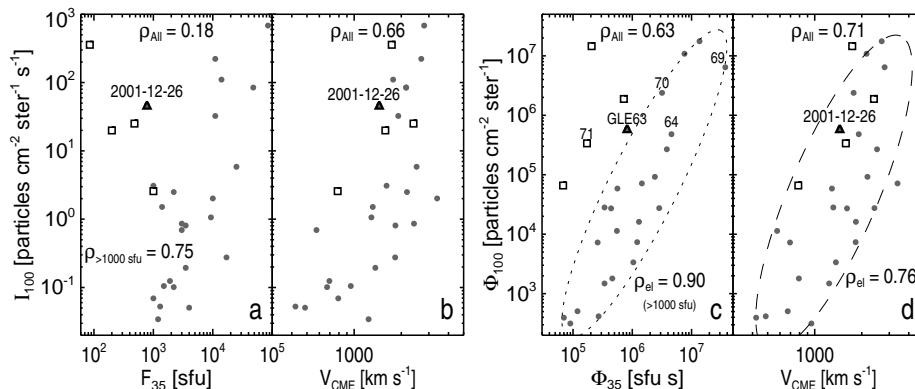


Figure 3. Near-Earth high-energy proton enhancements and strong microwave bursts recorded by NoRP at 35 GHz in 1996–2012. Scatter (log-log) plots present the longitude-corrected parameters of > 100 MeV protons (peak flux I_{100} in the left pair of panels, total fluence Φ_{100} in the right pair of panels) *versus* parameters of microwave bursts at 35 GHz (peak flux F_{35} left, fluence Φ_{35} right) and CME speed. The Pearson correlation coefficients at the tops of the panels were calculated for all 28 events (ρ_{All}), and those at the bottoms of panels c and d (ρ_{el}) are related to the events within the ellipses. The open squares denote the events with abundant proton outcome. The filled triangle denotes the 26 December 2001 GLE63 event. The GLE numbers are indicated at corresponding points in panel c.

The influence on the proton flux of the processes affecting their propagation from the source to detector (such as accumulation of trapped protons and velocity dispersion) can be compensated by considering their fluence. Figures 3c and 3d compare total proton fluences Φ_{100} with total microwave fluences Φ_{35} and V_{CME} . The broken ellipses enclosing the majority of the events are plotted by hand. The tilt of the major axis of each ellipse shows the trend, and its width represents the scatter. Note that the correlation coefficients rather than the scale-dependent eccentricities of the ellipses are significant.

Two groups of events show up. The first-group events with $F_{35} \geq 10^3$ sfu (gray circles) form a rather narrow cloud in Figure 3c within the dotted ellipse with a correlation coefficient as high as 0.90. The five proton-abundant events of the second group (with $F_{35} \leq 10^3$ sfu) remain isolated, although they approach the main cloud of points. On the other hand, the main cloud of points within the dashed ellipse in Figure 3d includes almost all abundant events (three open squares and the triangle of our event). Their arrangement nearly along its major axis corresponds to the main trend. The only exception is a big 8–9 November 2000 SEP event (*e.g.* Lario, Aran, and Decker, 2009). It is located not far from the ellipse, being much closer to the main cloud of points than in Figure 3c. The correlation coefficient for the whole set of events is higher with the CME speed in Figure 3d than with the microwave fluence in Figure 3c, supporting a shock-related contribution.

An apparent interpretation of Figure 3c is that the well-correlated SEPs of the first group were dominated by the flare-related acceleration, because the total number of protons depends on both the intensity and duration of the acceleration process. The correspondence between these parameters of the acceleration process and microwave burst is obvious, but not expected, if protons are accelerated

by shock waves far away from a flare region. The shock-related acceleration seems to dominate in the proton-abundant events of the second group. Nevertheless, their location closer to the main cloud of points in Figure 3c relative to Figure 3a supports the flare-related contribution in these events, too.

The asymmetry of flare magnetic configurations causes an additional scatter in the correlations between microwave bursts and SEPs. This asymmetry in the 26 December 2001 event reduced the microwave burst by a factor of two with the same production of accelerated particles (Article II).

GLE64, GLE69, and GLE70 fall within the ellipse in Figure 3c, which indicates their association with the first group. Detailed studies of the GLE69-related solar and particle event (Grechnev *et al.*, 2008a; Klein *et al.*, 2014) support the flare-related source of SEPs. The solar source event of GLE70 was similar to that of GLE69 (Grechnev *et al.*, 2013a) which also supports the indication of Figure 3c. GLE71 located away from the ellipse in Figure 3c and within the ellipse in Figure 3d looks like a shock-dominated event. GLE63 seems to have significant contributions from both flare-related and shock-related accelerations.

The high correlation for the first-group events within the ellipse in Figure 3c holds over three orders of magnitude for the microwave fluence and five orders for the proton fluence, while V_{CME} in Figure 3d range over one order of magnitude. A general pattern expressed by Kahler (1982) in terms of the BFS appears to be more complex than the correlation among all parameters in big flares. A general correspondence between the parameters of flares, CMEs, shock waves, and SEPs holds over a wide range of their magnitudes. According to Dierckx *et al.* (2015) and Trottet *et al.* (2015), the shock-related contribution statistically dominates at lower energies with a major role of flares at higher energies, where shock-accelerated SEPs also show up (Cliver, 2006; Gopalswamy *et al.*, 2015).

Based on these facts and considerations, contributions to the 26 December 2001 SEP event from both flare processes and shock waves may be expected. We use this assumption as a guideline in our analysis.

3. Eruptions

The eruptive flare on 26 December occurred in AR 9742 not far from the west limb (N08 W54). Figure 4a shows an EIT 284 Å image observed on 20 December, 130 hours before the event. The cross denotes the reported position of the flare. AR 9742 had a $\beta\gamma$ magnetic configuration. Approximate positions of the ends of the erupted flux rope and their magnetic polarities revealed by the flare ribbons and a magnetogram produced by *Michelson Doppler Imager* (MDI; Scherrer *et al.*, 1995) on SOHO (see Article II) are denoted S and N. A large S-polarity coronal hole opposite to AR resided in the southern hemisphere.

The EIT 284 Å image in Figure 4b presents the Sun on 26 December a few hours before the event. The southern coronal hole hidden by bright coronal structures rotated to the limb (it was visible again on 15–19 January 2002, when its area decreased). The black frame corresponds to the field of view in Figure 5, which shows the flare observed by TRACE in 1600 Å (see Article II for more details). The whole event consisted of the first flare (Figure 5a) and the main flare (Figure 5b).

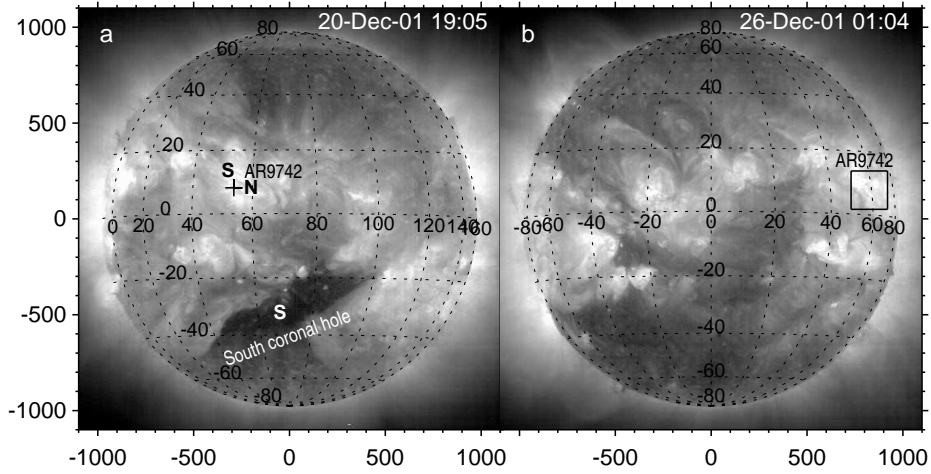


Figure 4. The overall situation on the Sun observed by SOHO/EIT in 284 \AA . (a) The Sun on 20 December. The reported position of the 26 December flare in AR9742 is denoted by the cross. A large coronal hole is present in the south hemisphere. Magnetic polarities S and N in the coronal hole and in AR9742 are indicated. The heliographic grid corresponds to the flare occurrence time. (b) The Sun on 26 December before the event. The black frame outlining the flare region corresponds to the field of view in Figure 5. The axes indicate the distance from solar disk center in arcseconds.

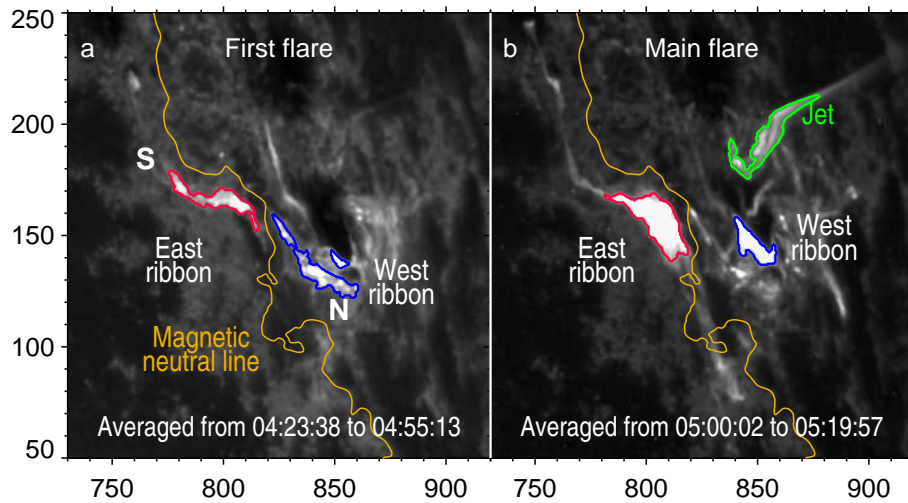


Figure 5. Two parts of the two-ribbon flare represented by TRACE 1600 \AA images averaged during the first flare (a) and main flare (b). The blue contours outline the west flare ribbons in the sunspot. The red contour outlines the east ribbon in a weaker-field region. The orange contour traces the magnetic neutral line computed from the SOHO/MDI magnetogram observed on 26 December at 04:51 (see Article II). Magnetic polarities S and N are indicated. The green contour in panel b outlines the brightest portion of the jet and a part of its base. The axes indicate the distance from solar disk center in arcseconds.

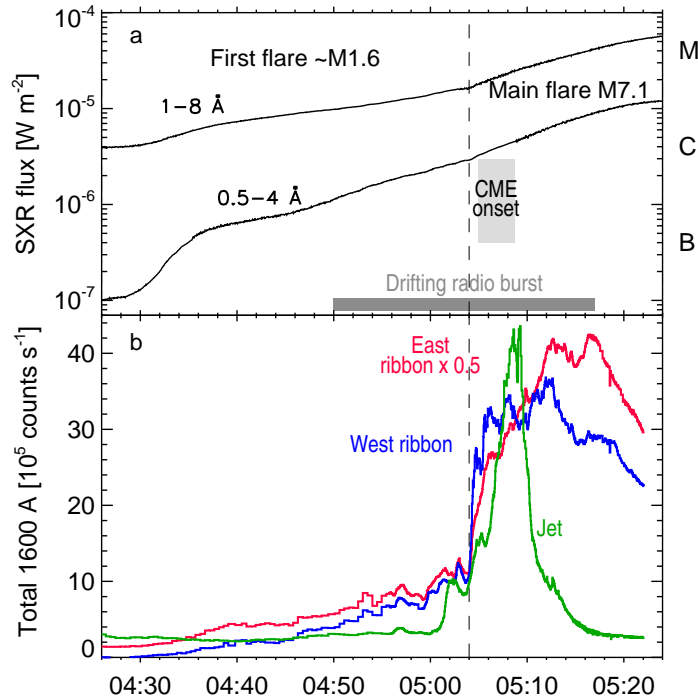


Figure 6. Flare light curves recorded by GOES in soft X-rays (a) and those computed from TRACE 1600 Å images in Figure 5 over the flaring regions presented with the corresponding colors (b). Two flare parts are separated by the dashed-vertical line. The gray bars in panel a represent the observation interval of a slowly drifting radio burst and the CME onset time extrapolated to the position of AR 9742.

3.1. First Eruption

The first, most likely eruptive flare started from the appearance of two long, thin, strongly sheared ribbons (Figure 5a). The west ribbon was close to the sunspot. The east ribbon was located in moderate magnetic fields. The SXR flux in Figure 6a started to rise after 04:30 and reached a GOES importance of about M1.6 at 05:04. Figure 6b shows the time-profiles computed from the TRACE 1600 Å images over the major regions outlined in Figure 5 with corresponding colors. Both ribbons gradually brightened by 05:04.

A slowly drifting Type II and/or Type IV burst in an interval marked in Figure 6a could only be caused by an expanding ejecta or wave from AR 9742, which started, at least, ten minutes before the main fast CME. Manifestations of the first eruption in running-difference EIT 195 Å images are presented in Figure 7. The top of a faint off-limb loop-like feature E1 in the pre-eruption image (Figure 7a) is outlined by the black arc. This top is displaced slightly in the initiation phase at 04:34:52 in Figure 7b and strongly in Figure 7c at 04:46:52, when it accelerated and brightened. Its lift-off apparently stretched closed coronal structures lying above. A dark dimming-like region above the limb started developing behind E1. The images in Figure 7 provide the projected heights of E1 at the three times.

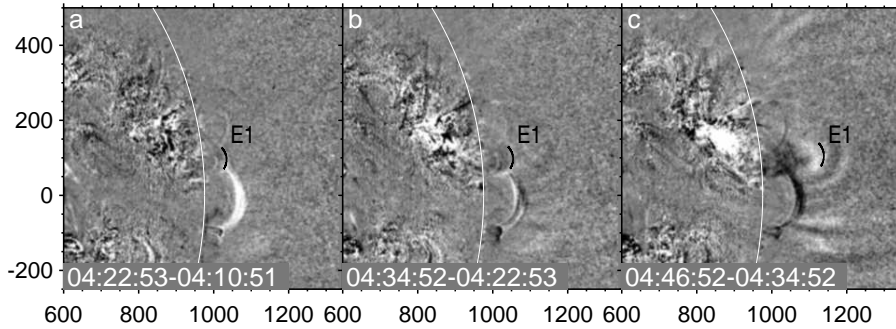


Figure 7. First eruption in running-difference EIT 195 Å images. (a, b) Slow expansion of coronal structures in the initiation phase. The black arc denoted E1 outlines the visible top of the rising structures. (c) Manifestations of the eruption in the stretched coronal structures. The axes indicate the distance from solar disk center in arcseconds.

3.2. Main Eruption

The main flare started at 05:04, close to the estimated CME onset time (light-gray bar in Figure 6a; see Article II). Emissions from both ribbons in 1600 Å and microwaves strongly increased. The west ribbon reached the sunspot umbra and partly covered it. The east ribbon lengthened and broadened into weaker-field regions. The SXR flux strengthened and reached an M7.1 importance at 05:40.

The EIT 195 Å difference image in Figure 8 reveals the traces of the associated main eruption, which occurred between 04:47 and 05:22. The onset time of the main flare and CME falls within this interval. Coronal structures are strongly disturbed. A large dimming surrounded by stretched loops appears above the limb. The flare configuration is not recognizable in the EIT image because of the low brightness threshold applied to detect faint surrounding features. A two-ribbon structure and bright jet are visible in a high-resolution TRACE 1600 Å image in the inset, whose actual position is denoted by the white frame.

3.3. Jet

A jet (green in Figures 5 and 6b) appeared after 05:06 from a funnel-like structure, while brightenings ran along its circular base. The time-profile of the jet in 1600 Å reached a peak at about 05:09, being as short as three minutes at half-height. Figure 9 presents the jet-like eruption. A combination of an EIT 195 Å image and an averaged TRACE 1600 Å image in Figure 9a reveals a large-scale configuration, where the jet occurred. Figure 9b presents a small-scale configuration, from which the jet emanated. This is an enlarged variance image of the jet computed from the TRACE 1600 Å images in an interval from 05:08 to 05:15. This image represents all changes occurring in this interval according to their statistical contributions (Grechnev, 2003).

The coronal configuration in Figure 9b resembles an inverted funnel. Such funnels appear above photospheric magnetic islands inside opposite-polarity regions and contain coronal null points (Masson *et al.*, 2009; Meshalkina *et al.*, 2009).

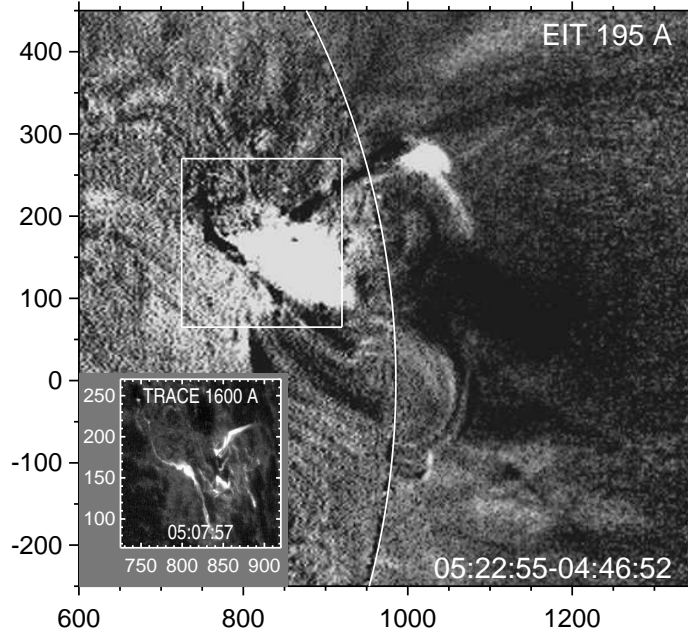


Figure 8. Traces of the main eruption in the EIT 195 Å difference image. The inset presents a TRACE 1600 Å image near the flare peak. Its actual position is denoted by the white frame. The axes indicate the distance from solar disk center in arcseconds.

The presence of a magnetic island at the photospheric base of the jet was revealed in Article II. A long tube-like extension (dark in the EIT image in Figure 9a) connects the ring base of the funnel with a remote magnetically conjugate region far away from AR 9742. The magnetic structure of a small flux rope erupting inside a funnel cannot survive when passing a null point (Uralov *et al.*, 2014), and released plasma flows out as a jet (Filippov, Golub, and Koutchmy, 2009). Jet-like eruptions in such configurations are characterized by ring-like ribbons, brightenings running along them, and impulsive temporal profiles.

Two compact brightest regions 1 and 2 in Figure 9b exhibited the largest variations. The temporal profiles computed over the whole jet and regions 1 and 2 are shown in Figure 9c. They demonstrate that coronal region 1 and region 2 in the base of the jet exhibited a simultaneous brightening as short as 20 seconds, suggesting a sharp impulsive energy release at about 05:09. This pulse, the preceding collision of the flux rope with the separatrix surface of the funnel, and a pressure pulse produced in the bend of the long tube-like structure by the injected dense material of the jet result in a strong impulsive disturbance excited by the jet around 05:09. The shock-wave excitation by a similar jet-like eruption was demonstrated previously by Meshalkina *et al.* (2009) and Grechnev *et al.* (2011).

In summary, the whole event comprised three eruptions. The first eruption indicated by the first two-ribbon flare and a slowly-drifting radio burst occurred around 04:35. The second, main eruption associated with the fast CME occurred around 05:04. The third, jet-like eruption was actually observed around 05:09.

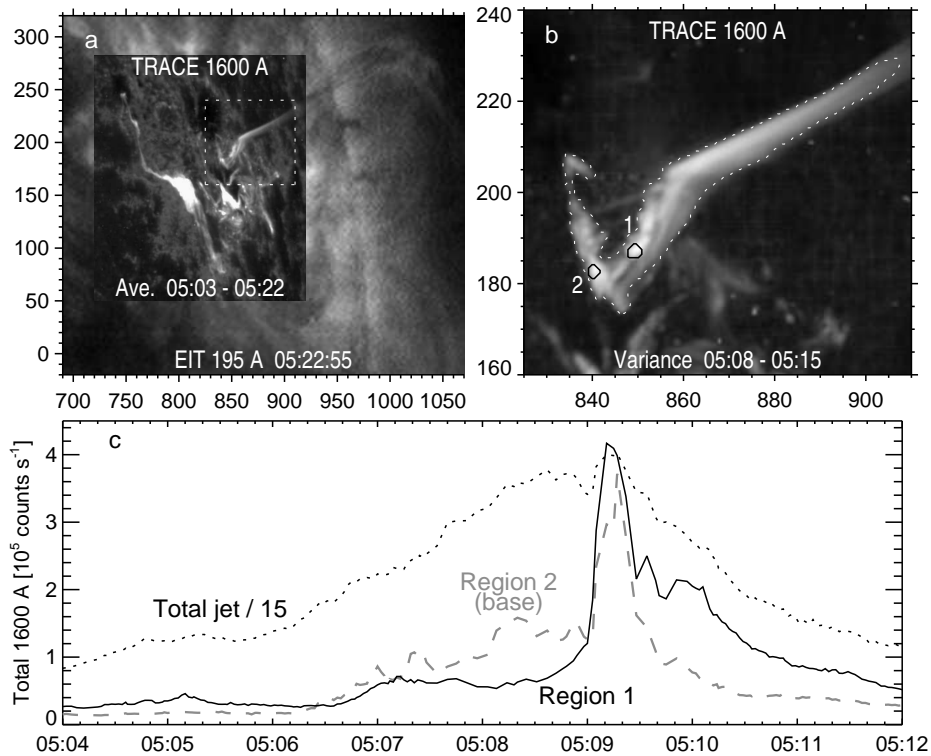


Figure 9. (a) The overall configuration of the jet in an EIT 195 Å image with an inserted averaged TRACE 1600 Å image. A jet visible in 1600 Å occurred in a long loop-like structure visible in 195 Å. (b) Variance map of the jet produced from the TRACE 1600 Å images during 05:08–05:15. The field of view corresponds to the white dotted frame in panel a. Labels 1 and 2 denote sharply brightened regions. The axes in panels a and b indicate the distance from solar disk center in arcseconds. (c) Temporal profiles over the whole jet within the dotted contour (reduced by a factor of 15) and those of the small regions 1 and 2 denoted in panel b.

4. Drifting Radio Bursts

To find further information about the eruptions and shock wave in our event, we consider dynamic radio spectra in a wide frequency range. The structures visible in dynamic spectra reveal non-thermal electrons streaming along open magnetic fields (Type III bursts), tracing the fronts of shock waves (Type II bursts), or confined in quasi-static or expanding magnetic structures (Type IV bursts).

4.1. Type II Bursts

To analyze Type II bursts, we use our technique to outline their trajectory verified in studies of several events. The trajectory is governed by the plasma density distribution in the way of a propagating shock wave. A freely propagating blast-wave-like shock, which spends energy to sweep up the plasma with a radial power-law density falloff, $n(x) \propto x^{-\delta}$ (x is the distance from the eruption center),

has a power-law kinematic behavior, $x(t) \propto t^{2/(5-\delta)}$ vs. time $[t]$ (Grechnev *et al.*, 2008b). The power-law density model, $n(h) = n_0(h/h_0)^{-\delta}$, with $[h]$ being the height above the photosphere, $n_0 = 4.1 \times 10^8 \text{ cm}^{-3}$, $h_0 = 100 \text{ Mm}$, and $\delta = 2.6$ is close to the equatorial Saito model (Saito, 1970) at $h \geq 260 \text{ Mm}$, providing a steeper density falloff at lower heights. The low-corona density increase corresponds to strongly disturbed conditions just before the appearance of the wave.

The expected trajectory of a Type II burst caused by the passage of the shock front through a structure with a decreasing density is a gradual monotonic curve. It has a steep onset and decreasing frequency drift with a convexity governed by the δ -parameter. The wave onset time $[t_0]$ usually corresponds to the rise of the HXR or microwave burst or precedes it by up to two minutes.

In practice, we choose a reference point on the dynamic spectrum at time t_1 , calculate a corresponding distance x_1 from our density model, and we adjust t_0 and δ (typically $\delta \approx 2.5 - 2.9$) in sequential attempts to reach best fit to bright Type II signatures of a trajectory calculated from the equation $x(t) = x_1[(t - t_0)/(t - t_1)]^{2/(5-\delta)}$ and plotted on top of the dynamic spectrum. Their visual comparison provides a typical accuracy of about 0.01 for δ and within one minute for t_0 . We also use this approximation to fit different wave signatures such as ‘‘EUV waves’’ and leading edges of fast CMEs (Grechnev *et al.*, 2011, 2013a, 2014b, 2015b, 2016). Note that the dynamic spectrum alone does not allow us to refer the density to a certain height, being basically insensitive to a constant multiplier $[n_0]$ of any density model.

Figure 10 presents a dynamic spectrum consisting of a *Hiraiso Radio Spectrograph* (HiRAS) spectrogram above 180 MHz and Learmonth data below 180 MHz in Figure 10b, and a spectrogram produced by the Rad2 receiver of the *Radio and Plasma Wave Investigation* (WAVES; Bougeret *et al.*, 1995) on the *Wind* spacecraft in Figure 10d. Figure 10a also shows a microwave burst at 17 GHz (NoRP: black) and 2.7 GHz (Learmonth: pink, late part only) as well as the total emission in 1600 Å from the west ribbon and jet (same as in Figure 6b).

An enlarged part of the Learmonth spectrogram in the inset (Figure 10c; the white frame denotes its actual position) reveals two harmonic pairs of Type II lanes crossing each other. The pair (1_F, 1_H), outlined by the dotted lines, is band-split. The pair (2_F, 2_H), outlined by the dashed lines, has a faster frequency drift. Adjustment of the wave onset time and density falloff exponent for each of the two paired bands indicates their relation to two different shock waves following each other. The first shock wave started at $t_{01} = 05:04:00$ ($\delta_1 = 2.65$) and was caused by the main eruption, while the second shock wave ($t_{02} = 05:09:10$, $\delta_2 = 2.54$) was produced by the jet (*cf.* Figure 10a).

Figure 11a shows a schematic of the two shock fronts at two times. The background is an EIT 195 Å image ratio between 05:22:55 and 04:46:52 inserted into an averaged white-light image from the Mark 4 coronameter (MLSO) observed on 27 December from 18 to 22 UT. The thick fronts correspond to the onset of Type II-1 (05:12:00) and the thin fronts correspond to the observation time of the EIT 195 Å image (05:22:55). Because of the lack of data required for correct reconstruction of the wave fronts, their shape is back-extrapolated from LASCO

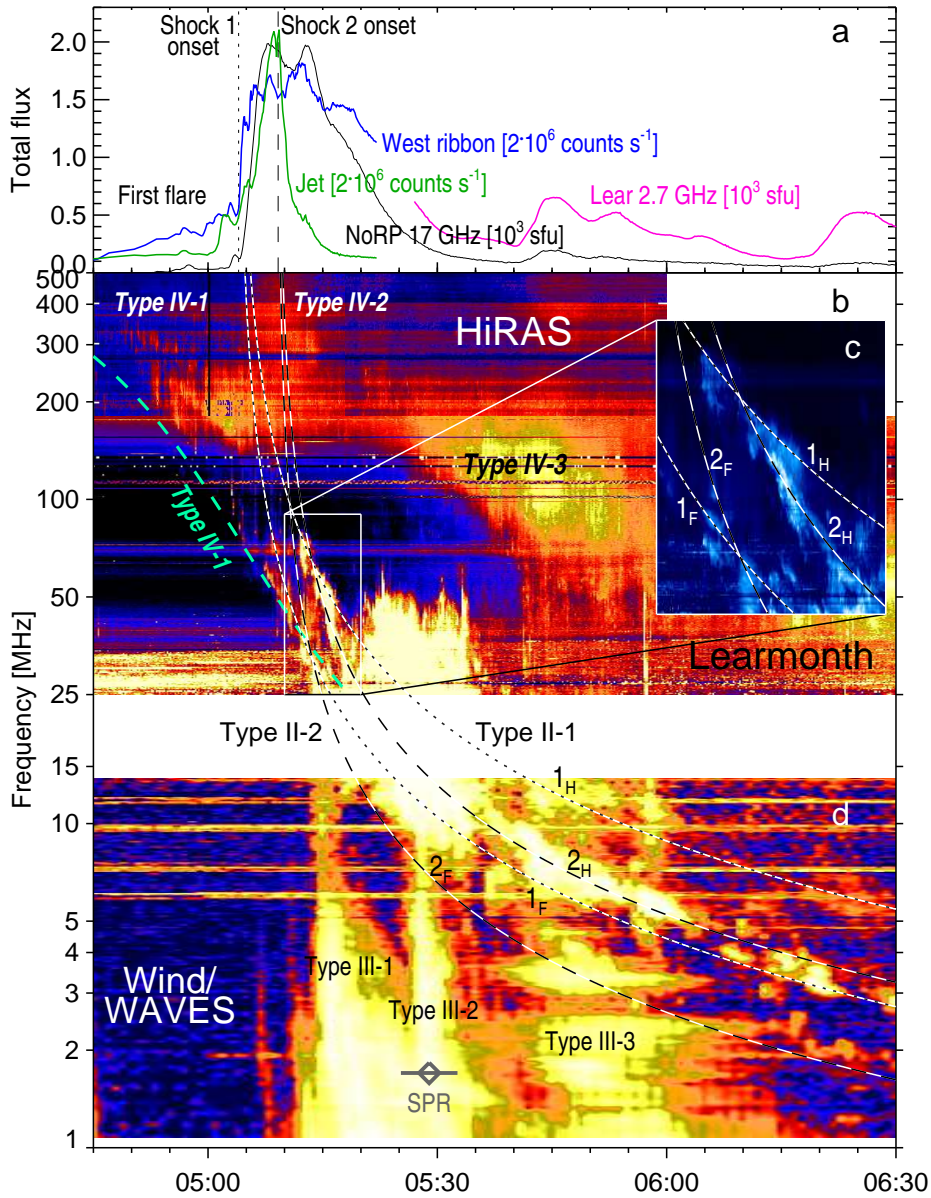


Figure 10. Combined dynamic spectrum (b and d) in comparison with the flare light curves (a). The vertical-broken lines in panel a represent the onset times of shock 1 ($t_{01} = 05:04:00$) and shock 2 ($t_{02} = 05:09:10$). Inset (c) presents an enlarged part of the Learmonth spectrogram denoted by the white frame. The slowly drifting radio bursts are outlined with calculated trajectories. The dashed-green curve (not shown in the inset) outlines the low-frequency envelope of Type IV-1 above 25 MHz. Traces of Type II-1 are outlined by the pair of dotted lines ($\delta_1 = 2.65$), and those of Type II-2 are outlined by the paired dashed lines ($\delta_2 = 2.54$). The gray diamond at the bottom labeled SPR denotes the estimated SPR time with an uncertainty represented by the gray bar (Reames, 2009b).

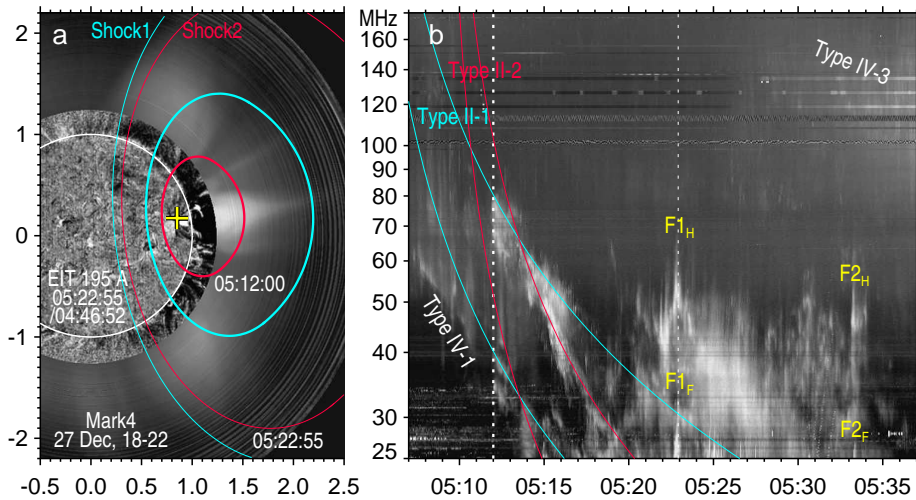


Figure 11. Two shock fronts in the corona (a) and the structure of the Type II burst (b). (a) A collage composed from an EIT 195 Å image ratio and a white-light image from the Mark 4 coronameter (MLSO). The color curves represent the global fronts of shock 1 (blue) and shock 2 (red) at 05:12:00 (thick) and 05:22:55 (thin). The yellow cross marks the eruption center. The white circle corresponds to the solar limb. The axes indicate solar radii from solar disk center. (b) The dynamic spectrum (Learmonth) with the main trajectories of the Type II-1 (blue) and Type II-2 (red) bands. $F1_H$, $F1_F$ and $F2_H$, $F2_F$ are harmonically related features. The vertical-dotted lines denote the times of the shock fronts in panel a.

images (Section 5) without crossing the solar surface, and their size is plotted roughly.

The Learmonth spectrogram in Figure 11b shows details of the Type II burst, which is saturated in Figure 10. Its bands partly shift after 05:18 to higher frequencies like an inverse N, indicating that a part of the shock front entered a denser region (see Grechnev *et al.*, 2011, 2014b). The Mark 4 image in Figure 11a really shows on the north and south broad dense regions, whose continuations should cross the solar disk. Two narrow-band harmonically related pairs $F1_H$, $F1_F$ and $F2_H$, $F2_F$ most likely belong to the Type II burst overlapping with Type IV and different emissions from 05:20 to 05:34. A Type III-like emission visible at 25–60 MHz between 05:24 and 05:28 has a different origin, because its enlarged structure shows irregular drifts. A later structure does not resemble Type III emission.

The EIT image ratio in Figure 11a reveals a large off-limb dimming visible behind the wave front. The dimming represents density depletion caused by plasma outflow after the passage of the shock wave, which upset the vertical hydrostatic equilibrium of the stratified atmosphere. The plasma flow behind the shock front swept away and stretched magnetic structures, increasing their volume. The plasma density near the solar surface dropped, while its height profile stretched in the streamer above AR 9742 visible in the Mark 4 image as well as a large dimmed corona. Thus, the second shock wave propagated in a modified corona with a flatter density profile, $\delta_2 < \delta_1$.

The drift rate $[df/dt]$ of the fundamental emission can be found from an equation $f = f_P(h, t)$ with f_P being the plasma frequency in the corona at a height h and time t corresponding to a portion of the shock front responsible for a Type II burst. Differentiation of this equation gives $df/dt = \partial f_P/\partial t + V_{\text{shock}} \partial f_P/\partial h \cos^m \alpha$, where V_{shock} is a phase speed of the shock front and α the angle between ∇f_P and the shock normal. Here $m = +1$, if the same portion of the shock front produces the Type II burst all of the time, and $m = -1$, if it is emitted by the intersection of the shock front with a coronal ray. If the coronal distribution $f_P = f_P(h)$ is stationary and $\alpha = 0$, then, with $f_P \approx 9 \times 10^3 n^{1/2}$ and $n = n_0(h/h_0)^{-\delta}$, we get $f' = df/dt \approx V_{\text{shock}} \partial f_P/\partial h = -\delta V_{\text{shock}} f(f/f_{P0})^{2/\delta}/(2h_0)$. With $f_{P0} = f_P(n_0) = 182$ MHz and the frequency-drift rates of the fundamental emission for shock 1 $[f'_1]$ and shock 2 $[f'_2]$ at their intersection in Figures 10 and 11b (05:13:30, $f \approx 33$ MHz), we estimate an instantaneous ratio of their speeds at that time $V_{\text{shock}2}/V_{\text{shock}1} \approx (\delta_1/\delta_2)(f'_2/f'_1) \times (f/f_{P0})^{(2/\delta_1 - 2/\delta_2)} \approx (2.65/2.54) \times 2 \times (33/182)^{-0.033} \approx 2$. The height of the Type II-2 source was different from that of Type II-1 at that time, because shock 2 propagated in the corona modified by shock 1.

Continuations of the trajectories in Figure 10 to the frequencies < 25 MHz are not obvious because of the gap between the HiRAS and Learmonth and *Wind*/WAVES bands and complex structures of the Type II bursts. The identification of the bands in the *Wind*/WAVES spectrogram is not guaranteed, while the calculated trajectories match the actual evolution of the frequency drift. The *Wind*/WAVES spectrogram shows, at least, three Type II bands, confirming the presence of two shocks. Two shock waves following each other within a few minutes were observed previously (Grechnev *et al.*, 2011, 2013a).

The Type II emission in this event was observed up to a very low frequency of about 150 kHz. It is a long-standing issue if Type II emissions observed in the decametric/hectometric (DH) range and at still longer waves, also termed interplanetary (IP) Type II events, can be extensions of metric Type II bursts. An apparent mismatch between the trajectories of the former and latter events has been considered as an indication of different origins of responsible shocks.

In this view, Cane and Erickson (2005) examined several events and estimated that “ $< 15\%$ of the Type IIs extending below 15 MHz actually extend below 5 MHz and that the lowest frequency extent is about 1 MHz”. The authors found “no clear example of a metric Type II burst that extends continuously down in frequency to become an IP Type II event” at lower frequencies. The 26 December 2001 event was specially considered by the authors with the conclusion “like other events, there is a disjoint in frequency between the Type II burst and emission likely to be related to the CME shock [*i.e.* IP Type II event]”.

To understand if our analysis can shed light on this problem, we extend our outline of the two shock waves from Figure 10 up to 100 kHz. Because Cane and Erickson (2005) were concerned about the proper frequency scaling of concatenated spectrograms (here *Wind*/WAVES Rad2 + Rad1), we have taken their Figure 13 and plotted over it our trajectories found from the metric Type II bursts without any additional adjustment. Figure 12 shows the result. The white-on-black frame in the top-left corner represents the field of view in Figure 10. Continuation of the metric Type II burst is visible until 10:00. Then the Type II

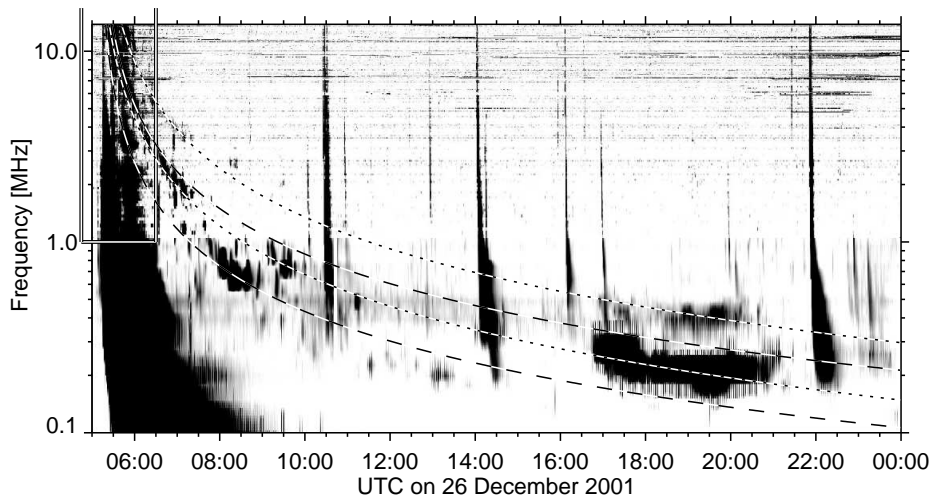


Figure 12. Interplanetary Type II event in a *Wind*/WAVES Rad2 + Rad1 spectrogram (adapted from Cane and Erickson, 2005. Courtesy H.V. Cane). The pairs of broken lines represent the same calculated trajectories of two shock waves following each other, shock 1 (dotted) and shock 2 (dashed), as in Figure 10. The white-on-black frame represents the range shown in Figure 10.

emission reappeared at about 17:00 along the same calculated trajectories. This correspondence confirms its persistent origin. It is not clear if the Type II emission was interrupted because of unfavorable conditions for its generation or propagation issues.

Although the Type II bands are not continuous and their identification is not guaranteed, the calculated trajectories correctly reproduce the actual evolution of the frequency drift throughout the event in the whole frequency range without any frequency mismatch between the metric and IP Type II emission. The impression of a mismatch was probably caused by a complex structure of the radio emission with gaps between the Type II portions observed and the presence of misleading features, which might be irrelevant to the main trajectories.

Figure 12 also leads to the following conclusions: i) The Type II emission in the whole range where it was observed, from about 80 MHz to about 150 kHz, was due to the same shock wave, which was excited by the eruption in AR 9742 during the flare; ii) The Type II bands and blobs in the 0.5–5 MHz range between 06:30 and 10:00 corresponding to different dotted and dashed trajectories certify the presence of two different sources of the Type II emission. This fact rules out a popular idea relating the Type II source to the bow-shock ahead of the CME nose. At least one of the radio sources must be located at a flank of the shock wave, because two bow-shocks cannot be driven by a single piston. Most likely, two lateral blast-wave-like shocks coexisted, at least until 09:00, while ahead of the CME they merged into a single stronger shock (Grechnev *et al.*, 2011).

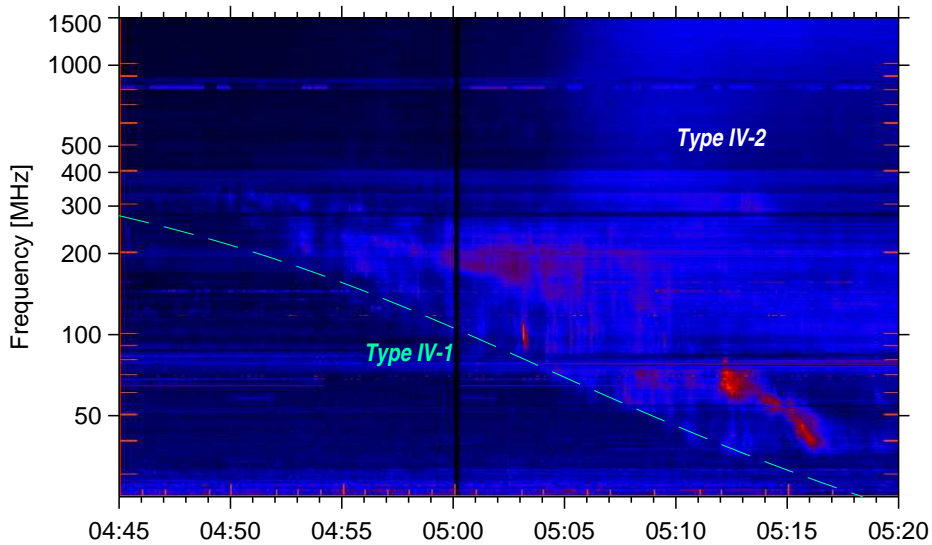


Figure 13. Type IV bursts in the HiRAS spectrogram. The dashed-green curve (same as in Figure 10b) outlines the low-frequency envelope of Type IV-1 according to the height–time plot in Figure 14a.

4.2. Type IV Bursts

A slowly drifting burst visible in Figure 10b from 04:50 until 05:13 outlined from below by the dashed-green line resembles a Type II burst. So it was reported by some observatories and considered by Nitta *et al.* (2012). However, the convexity of its trajectory with an increasing drift rate is opposite to those of Type II-1 and Type II-2. The structure of this burst is better visible in Figure 13, which presents an adapted HiRAS spectrogram (2001122605.gif) accessible at sunbase.nict.go.jp/solar/denpa/hirasDB/Events/2001/.

At first glance, the burst comprised a pair of bands with a frequency ratio of 1.8 (the bright red feature visible from 05:12 to 05:16 between 40 and 80 MHz is due to Type IIs). Its spectrum is cut off towards lower frequencies, as expected for a population of confined electrons. The high-frequency cutoff has a less pronounced drift, if any, so that the bandwidth of this burst increases, which does not resemble a Type II burst. This burst, Type IV-1, suggests emission from an electron population confined in an expanding magnetic structure.

The second broadband burst in Figure 13, Type IV-2, started about 05:05 in association with the main eruption. Its quasi-stationary high-frequency part, probably related to the flare arcade, extended up to > 2000 MHz and lasted until 05:27. The HiRAS spectrogram suggests a drift of its low-frequency part to lower frequencies (invisible in Figure 10b). A slowly drifting burst Type IV-3 superposed on a Type III group appears in Figure 10b much later, probably due to emission from the structures well behind the CME leading edge.

Analysis of Type IV-2 and Type IV-3 is hampered by their poor visibility and overlap with different structures. We focus on Type IV-1. This slowly drifting burst evidences a moving source. The moving radio source is often observed

along the extrapolated trajectory of an erupting prominence (see, *e.g.*, McLean, 1973; Klein and Mouradian, 2002). By relating a drifting Type IV burst to the observed expansion of an SXR source, Grechnev *et al.* (2014b) reconstructed its kinematics in a time interval exceeding imaging observations.

It is not possible to use here either the density model or kinematics estimated from the analysis of Type II bursts, unlike the bow-shock regime, when the kinematics of the piston and shock is similar. The low-cutoff frequency of a Type IV burst is controlled by plasma in an expanding dense structure, while the frequency of a Type II burst is governed by its environment. The structure responsible for a Type IV burst accelerates starting from a small velocity; a shock wave responsible for a Type II burst starts from the fast-mode speed ($> 10^3 \text{ km s}^{-1}$ above an active region) and then decelerates. Most likely, the first eruption responsible for Type IV-1 has not produced a shock wave.

Following the approach of Grechnev *et al.* (2014b), we assume that the frequency drift reflects the decreasing density in an expanding volume with a size r and relate the low-cutoff frequency to the plasma frequency: $f_p \propto n^{1/2} \propto r^{-3/2}$. An additional indication is an expected similarity of the velocity–time plot of an eruption to the SXR flux (Zhang *et al.*, 2001; Grechnev *et al.*, 2014b, 2016). To relate the spatial and frequency (density) scales, we refer to the top of the first eruption revealed by the EIT images in Figure 7. The plane-of-sky measurements are corrected by a factor of $1/\sin \lambda$ for the longitude of AR 9742 [$\lambda = 54^\circ$].

We composed the acceleration time-profile from two Gaussian pulses, adjusting their parameters to make its antiderivative similar to the SXR flux and to reproduce the Type IV-1 envelope (see Grechnev *et al.*, 2011, 2013a, 2014b, 2016 for the description of the technique). The kinematical plots are presented in Figure 14. The calculated low-frequency envelope of Type IV-1 is shown in Figures 10b and 13 by the dashed-green line. The correspondence of the inferred kinematics to Type IV-1, SXR flux, and to the EIT images confirms its likelihood. In spite of uncertainties, it is clear that when the second eruption started, the first erupting structure has reached a height of about 600 Mm, being still not far away. It stretched closed loops ahead of the main erupting structure, and cleared the path for its expansion, thus facilitating its lift-off.

4.3. Type III Bursts

The *Wind*/WAVES spectrum in Figure 10d shows three strong Type III bursts. Type III-1 started at the high-frequency edge of the Rad2 passband around 05:15 and lasted within three minutes. Type III-2 started around 05:27 and had a similar duration. No metric Type III bursts are detectable before Type III-2. Conversely, Type III-3 corresponds to a clear group of metric Type IIIs in an interval of 05:40–06:00, when minor microwave bursts are visible at 17 GHz in Figure 10a. The sources of these bursts were also located in AR 9742 (Article I).

While acceleration of electrons in the flare region is manifested by the flare emissions in the whole interval of Figure 10a, the absence of metric Type IIIs until Type III-3 indicates isolation of the magnetic configuration in AR 9742 from the interplanetary space. Two minor Type IIIs in Figure 10d before Type III-1 are unlikely to be important. The configuration opened, when Type III-3 started.

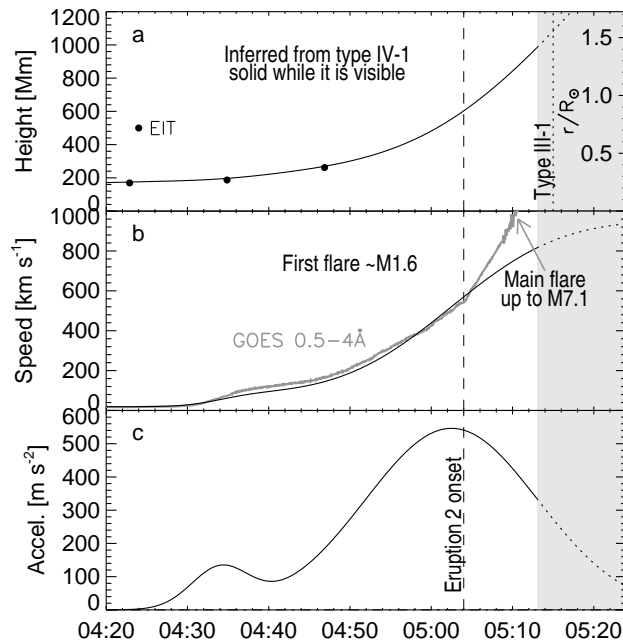


Figure 14. Kinematics of the first eruption (leading edge) in the radial direction inferred from the analysis of the Type IV-1 burst, SXR flux, and EIT data (filled circles from Figure 7). (a) Height–time plot. (b) Velocity–time plot along with a GOES SXR flux scaled to match the velocity. (c) Acceleration–time plot. Type IV-1 is detectable until the shading. The dashed-vertical line denotes the onset time of the second eruption. The dotted-vertical line in panel a denotes the onset time of the Type III-1 burst.

Type III-1, with a starting frequency between 14 and 25 MHz, was unlikely to have been caused by electrons escaping from the flare region. The only apparent source of non-thermal electrons is the expanding flux rope, which appeared in the first eruption and contained trapped electrons responsible for Type IV-1. Reconnection between this flux rope and an open structure such as a streamer (Grechnev *et al.*, 2013a) or coronal hole (Masson, Antiochos, and DeVore, 2013) could create a path for electrons trapped in the flux rope to escape into interplanetary space (Aschwanden, 2012). Besides electrons, protons and heavier ions, both pre-existing in the flux rope and injected into it in the course of flare reconnection, from thermal and suprathermal up to high energies, were released. A rich seed population was supplied for acceleration by a trailing shock wave. The presence of the Type IIIs in the whole frequency range of *Wind*/WAVES shows that the particles released could reach the orbit of Earth.

The onset of Type III-1 (vertical-dotted line in Figure 14a) corresponds to a height of the flux-rope of $\approx 1.55 R_{\odot}$. Reconnection between the flux rope and a streamer or coronal hole could occur at a farthest edge of the flux-rope’s flank, at a height of $\approx 0.78 R_{\odot}$ for a circular geometry. Our power-law density model does not help here, because the density multiplier [n_0] is unknown. The plasma frequency expected at this height is 30 MHz in a streamer (Newkirk, 1961) and

8.6 MHz in a coronal hole (Saito, Poland, and Munro, 1977) *vs.* expected 14–25 MHz. Either option is possible with our uncertainties.

While the height–time plot of the second flux rope formed in the main eruption is unknown, a similar scenario associated with Type III-2 is indicated by Type IV-2 related to the main flare and its probable drift to lower frequencies; the starting frequency of Type III-2 between 9 and 25 MHz, similar to that of Type III-1, without metric counterparts; and a probable opening of the magnetic configuration after Type III-2. The second flux rope could reconnect with the same open magnetic structure as the first one and at a comparable height.

The particles accumulated in the second flux rope in the course of a stronger main flare were released after the Type III-2 onset. This population of particles must be more energetic and plentiful. The estimated SPR time (Reames, 2009b: the gray diamond labeled SPR) coincides with Type III-2. The first particle release during Type III-1 does not contradict the GLE onset 12 minutes earlier than the estimated SPR time (the dashed line in Figure 2b); thus, energetic particles accelerated in the first flare could directly contribute to the SEP event.

Type III-3 indicates direct escape of electrons (and probably other particles) from the flare region evidenced by a group of the corresponding metric Type IIIs. The peak of the microwave spectrum shifted from 6 GHz (Article II) to ≈ 2.7 GHz at that time, as comparison of the burst at 17 GHz (black) and 2.7 GHz (pink) in Figure 10a shows. This suggests displacement of the microwave-emitting region (and, possibly, the site of flare energy release) to weaker magnetic field at larger altitude. These late-stage processes might be related to the post-impulsive particle acceleration (see, *e.g.*, Chertok, 1995; Klein *et al.*, 1999, 2014). It is possible, but questionable, that the released particles were accelerated by a shock wave.

5. White-Light CME

A white-light transient was observed by the LASCO-C2 and -C3 coronagraphs starting from 05:29 up to $30 R_{\odot}$. The transient consisted of a structured CME body (probable flux rope) surrounded by a faint partial-halo wave trace. The same LASCO images in Figure 15 processed in different ways reveal CME structures (top) and wave traces (bottom, running differences), which are detectable from a diffuse halo-like brightening or deflected coronal rays.

The sky-plane expansion of the CME body and wave was very similar. We therefore fitted the kinematics of both with the same power-law appropriate for a shock wave. The wave onset time, $t_0 = 05:10:00$, is slightly later than that of shock 2 ($t_{02} = 05:09:10$). This corresponds to an expected coalescence of two shock waves into a stronger one with an apparently later onset time (Grechnev *et al.*, 2011). The power-law exponent is $\delta = 2.57$, close to the mid-latitude Saito model, which describes the corona above the quiet Sun (different values of δ found in Section 4.1 for the Type II burst were related to a streamer). The kinematical plots are shown in Figures 16a and 16b by the solid lines. Using these kinematics, the images in Figure 15 are progressively resized to maintain the visible size of the expanding transient (see also the 2001-12-26_LASCO.mpg movie in the Electronic Supplementary Material).

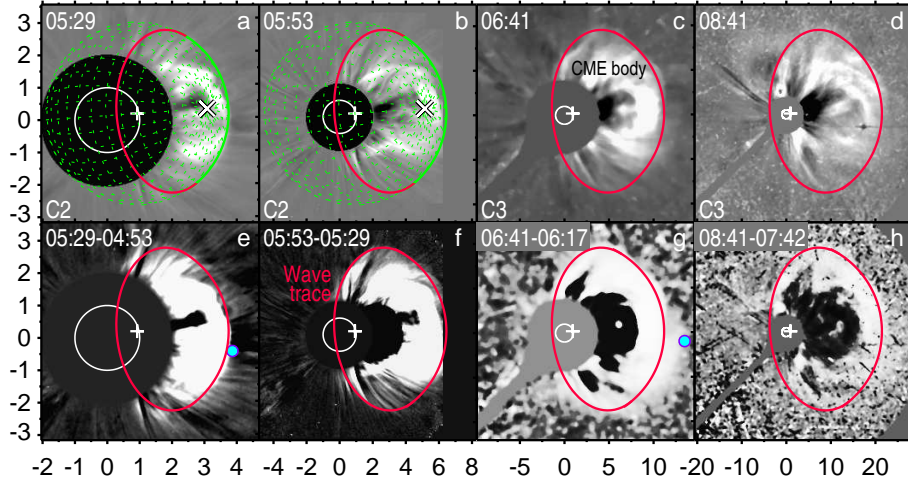


Figure 15. CME body (top) and wave traces (bottom, running differences) in LASCO-C2 and -C3 images. Panels a and b explain the calculations of the wave outline (red in other panels). A bulge protruding southwest is visible in later images. The blue-filled circles in panels e and g denote the measurements in the CME catalog corresponding to the bulge. The axes indicate the distance from solar disk center in solar radii.

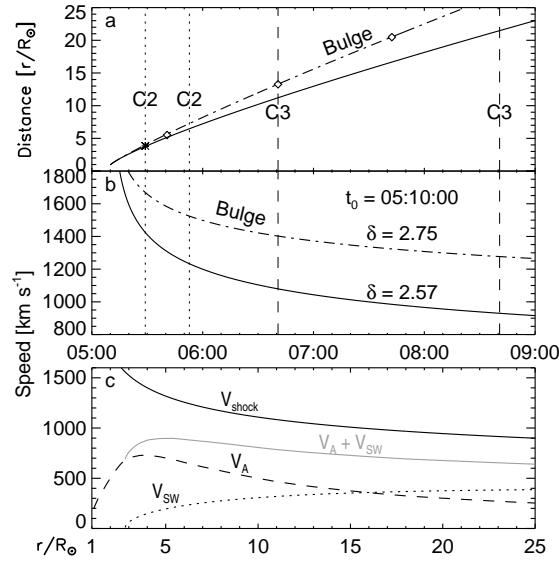


Figure 16. Kinematic plots of the transient visible in LASCO images. (a) Height–time plots for the main envelope of the CME leading edge (solid) and for the bulge (dash–dotted). The symbols represent the measurements from the CME catalog. (b) Speed–time plots for the main CME envelope (solid) and the bulge (dash–dotted) calculated for a decelerating shock wave with the same onset time, $t_0 = 05:10:00$, and different density falloff exponents δ . (c) Distance–velocity plot for the main CME envelope (black solid) corresponding to the wave along with the models of the Alfvén speed V_A (dashed) and solar wind speed V_{SW} (dotted) above the quiet Sun. The gray curve represents the sum $V_A + V_{SW}$.

Figures 15a and 15b explain how the shape of the wave front was calculated. Green is a sphere centered at the eruption site (straight cross), with a polar axis extending its radius-vector (slanted cross marks the pole), and a radius taken from Figure 16a. Red is a small circle on this sphere (its plane does not pass through the sphere's center). The red curve in the other panels of Figure 15, composed from the red and green arcs in Figures 15a and 15b, matches most wave traces in all images. Thus, the main part of the wave front is a conic section of the sphere, as expected for a blast wave. The deflected rays outside of the outline in Figure 15e are most likely due to the flanks of the earlier shock 1 ($t_{01} = 05:04$). Two shock waves running across the solar disk one shortly after another were observed previously (Grechnev *et al.*, 2013a).

Figure 15g reveals a southwest bulge ahead of the red outline, which might be ascribed to a bow-shock, but its orientation is offset from the main expansion direction of the CME. Correspondence of the bulge to the position of a large coronal hole in Figure 4 indicates its relation to the fast solar wind stream from the coronal hole. The measurements in the CME catalog (cdaw.gsfc.nasa.gov/CME_list/; Yashiro *et al.*, 2004) are related to the bulge. They are denoted by the symbols in Figure 16a and outlined in Figures 15a and 15b by a power-law fit with a steeper $\delta = 2.75$ expected for a coronal hole.

Figure 16c presents the velocity *vs.* distance (black solid) of the main CME envelope related to the spherical wave front (without the bulge). This is a power-law fit for the apex of the observed wave front. For comparison, the dashed curve represents a model for the Alfvén speed $[V_A]$ above the quiet Sun (Mann *et al.*, 2003). The dotted curve shows a model for the solar-wind speed $[V_{SW}]$ (Sheeley *et al.*, 1997). If a wave is weak, then its velocity is $V_{SW} + V_{fast}$ with V_{fast} being the fast-mode speed. The head of the wave front moves at distances $5 - 25 R_\odot$ practically along the magnetic field, *i.e.* $V_{fast} \approx V_A$ (V_A exceeds the sound speed). The considerable excess over the Alfvén speed of the wave speed relative to the moving environment $V_{shock} > V_A + V_{SW}$ (the gray curve shows the sum) confirms the shock-wave regime in the whole range of distances. The Mach number characterizing the wave intensity can be estimated as $M = (V_{shock} - V_{SW})/V_A$ (with increasing M this formula becomes inaccurate). The Mach number is $M \approx 1.6$ at distances $5 - 10 R_\odot$, whereas $M \approx 2$ at $25 R_\odot$.

In summary, the partial halo surrounding the CME body was most likely a trace of a shock wave, which had both blast-wave and bow-shock properties in the LASCO field of view from $3.8 R_\odot$ to $30 R_\odot$. The CME and wave were super-Alfvénic and expanded similarly (bow-shock), while their common kinematics and the spherical wave front corresponded to the impulsively excited blast wave, whose propagation was controlled by the growing mass of the swept-up plasma.

6. Discussion

6.1. Presumable Kinematics of the Fast CME

The results of the analysis allow reconstruction of the presumable kinematics of the fast CME. We also invoke the following conclusions and observational

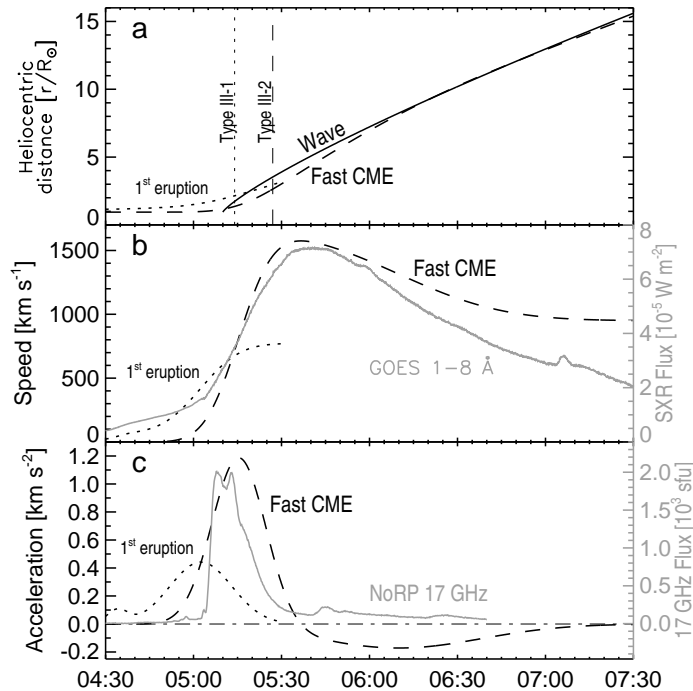


Figure 17. Presumable plane-of-the-sky kinematics of the fast CME (dashed) up to $15 R_{\odot}$ inferred from indirect indications. (a) Distance–time plot and a wave plot from Figure 16a (solid). (b) Velocity–time plot along with the GOES SXR flux (gray). (c) Acceleration–time plot and a microwave burst at 17 GHz (gray). The dotted curves correspond to the first eruption (Figure 14) inferred from the analysis of Type IV-1 and corrected to the plane of the sky. The broken vertical lines in panel a denote the onset times of the Type III-1 and Type III-2 bursts.

results: i) acceleration of a CME is synchronous with an HXR (or microwave) burst (Zhang *et al.*, 2001; Temmer *et al.*, 2008, 2010; Grechnev *et al.*, 2015b); ii) the velocity–time plot of a CME is similar to the SXR flux (Zhang *et al.*, 2001; Grechnev *et al.*, 2016); iii) the Neupert effect: the temporal profile of an HXR (microwave) burst is similar to the derivative of the SXR flux (Neupert, 1968); and iv) the height–time and velocity–time plots of the CME in the LASCO field of view should be close to those of the shock wave in Figures 16a and 16b (Section 5).

According to the last item, the initial impulsive acceleration of the fast CME should be followed by a deceleration phase, because the shock wave decelerated all of the time. We therefore composed the CME acceleration as a positive Gaussian pulse resembling the microwave burst followed by a negative pulse. The velocity should be roughly similar to the GOES 1–8 Å flux, being about 1000 km s^{-1} at 07:30. The result is shown in Figure 17 by the dashed curves. The dotted curves correspond to the first eruption (Figure 14 in Section 4.2) corrected to the plane of the sky by a factor of $\sin \lambda$ (with a longitude $\lambda = 54^{\circ}$). The CME and shock wave (solid lines) in Figure 17a are close to each other after 05:30, as expected.

The presence of two eruptions forming the CME complicates the situation. The flux rope ejected during the first flare eventually constituted the CME top part and the second flux rope joined it from below. The difficulties in untangling the kinematical plots of the two CME components result in the differences between the CME speed and SXR flux in Figure 17b and between the CME acceleration and microwave flux in Figure 17c. The derivative of the SXR flux, which contains an increasing component from the first flare, is smoother than the 17 GHz burst. We have adopted a compromise shape of the acceleration somewhat smoother than the microwave burst and a corresponding velocity somewhat sharper than the SXR flux. The estimated acceleration peak (1.2 km s^{-2} in the plane of the sky and 1.5 km s^{-2} in the radial direction) is comparable with a radial acceleration of 1.1 km s^{-2} estimated by Gopalswamy *et al.* (2012) for this event from different considerations. Our value might still be underestimated; nevertheless, the plots appear to be acceptable with the uncertainties we have.

The CME plots in Figure 17 were reconstructed in the basis of recent results by referring to dynamic radio spectra and scarce imaging observations. These plots lead to the following conclusions discussed in the next sections.

- i) The acceleration of second flux rope corresponds to a typical impulsive piston. It must have excited a blast-wave-like shock not later than the acceleration peak. The second flux rope was below the first one at that time.
- ii) The second flux rope exceeded the first one in speed and acceleration by a factor of ≥ 2 and became super-Alfvénic before its observations by LASCO.
- iii) The heights reached by the first flux rope and the second one, when corresponding Type III bursts started, are comparable, being related as 1:1.35.

6.2. Shock Wave

6.2.1. Shock-Wave History

The observations found for this event fit within a scenario outlined in Section 1. The second flux rope formed by reconnection (also responsible for the flare) accelerated and produced a strong disturbance as an impulsive piston. The shock-wave excitation by the jet-like eruption was similar. The impulsive-piston scenario is well known – see, *e.g.*, Vršnak and Cliver (2008). A crucial factor for the shock formation not considered in this article is inhomogeneous distribution of the fast-mode speed. Propagating into environment of a much lower fast-mode speed, the disturbance undergoes jamming of its profile and must rapidly steepen into the shock (Afanasyev, Uralov, and Grechnev, 2013).

The impulsive-piston excitation of a shock wave and its properties resemble the expectations for the hypothetical ignition of a freely propagating decelerating blast wave by the flare pressure pulse. However, the role of the impulsive piston in the observed events is played by the erupting flux rope rather than the flare loops. The flare-ignition of shock waves is neither supported by observations nor expected from general considerations for the following reasons.

The pressure of the plasma in flare loops is controlled by its temperature and density, which determine the SXR emission of the loops. It is intrinsically

gradual and usually resembles the antiderivative of the HXR or microwave burst (the Neupert effect: Neupert, 1968). On the other hand, the HXR burst is similar to the acceleration pulse of an erupting structure, as several studies concluded (see Section 1). Thus, any erupting structure is generally an efficient impulsive piston, producing much sharper pressure pulse than the flare loops.

Even the situation with the plasma β in flare loops $\beta \approx 1$ is normal in a flare. The plasma-pressure increase caused by chromospheric evaporation is balanced by the dynamic pressure of the reconnection outflow. All dimensions of a flare loop increase by an inconsiderable factor of $\sqrt[4]{1+\beta}$ (Grechnev *et al.*, 2006). The disturbance is too weak to produce a shock wave. Our observational studies showed that the size of SXR-emitting flare loops does not change when a shock wave appears, and that its onset time is close to the acceleration peak of an erupting structure, which can precede the HXR peak by one to two minutes.

We found that shock waves were impulsively excited by sharply erupting flux ropes in eight events, when their kinematics were measured. These events range from the GOES B- to X-class and were or were not accompanied by non-thermal HXR and/or microwave bursts. The shock waves in these events and three others, in which their exciters were not measured, exhibited identical behaviors, initially resembling blast waves. In the events with fast CMEs, shock waves showed some properties of bow shocks only after some time. The pure bow-shock excitation scenario has not been found in any flare-related eruption. The bow-shock regime presumed in most studies of SEPs (Reames, 2009a; Aschwanden, 2012; Gopalswamy *et al.*, 2012; and others) is ruled out by the fact that two shock waves observed in two events followed each other within six minutes. The initial bow-shock excitation is not excluded for gradually accelerating non-flare-related CMEs.

The 26 December 2001 event associated with a major flare shows the same shock-wave history as the flare-related events studied previously. The first shock wave was impulsively excited by the main eruption at 05:04. The second shock wave was similarly excited by the jet at 05:09. Both shock waves following each other initially resembled decelerating blast waves. The trailing front must have reached the leading one around the radial direction and merged with it into a stronger one with a later onset time at 05:10. As Section 5 concluded, the partial halo surrounding the CME body was a trace of a shock wave, whose properties in the LASCO field of view were intermediate between the blast wave and bow shock.

6.2.2. Regimes of Shock Waves

The solid curve in Figure 16c is a power-law fit of the measured shock-wave speed and formally corresponds to a solution of a self-similar blast wave in plasma with a power-law density *vs.* distance dependence. The mass of plasma involved in the motion continuously grows. The integral of the kinetic energy is conserved, as well as the integral of the sum of the plasma thermal energy and magnetic-field energy within the volume behind the shock front. Conservation of both energy integrals in this regime suggests an increasing impulse of the mass moving within a fixed solid angle, if the density falls off no more steeply than r^{-3} (to have a finite initial mass). The impulse increases because of a considerable pressure

difference upstream and downstream of the shock front. The system consisting of the CME and associated shock possesses such properties. The initial impulse of the system is zero, the total mass of the moving gas grows, and the impulse increases due to magnetic driving forces responsible for the development and expansion of the CME. This situation persists up to some distance. Our power-law fit applies to the position and speed of the decelerating shock front at this stage.

The magnetic driving forces, which initially increased the CME impulse, weaken with an increasing distance from the Sun. The outer magnetic influence on the CME and disturbed solar wind ceases. The total impulse of the system starts being conserved. The CME deceleration is governed by the interaction regime of the CME with the solar wind. Two extremities are possible: i) flow around the CME without change in its mass and ii) the “snowplow” regime, when the mass of the CME moving by inertia grows because of adhesion of the solar wind plasma to the CME instead of flowing around it. The change in the CME impulse in either regime is equal (but opposite) to that of the solar wind. The total drag force is equal to the time-derivative of this impulse and can be calculated. We do not consider the “snowplow” regime, which results in a much stronger deceleration than the solid curve in Figure 16c shows. The mass increase is unlikely at large distances from the Sun, where the CME expands radially.

Two situations of the flow around the CME are possible: i) the solar-wind flow rapidly recovers behind a compact CME and ii) the disturbed zone behind the CME is much larger than that ahead of it. The drag force is absent in the idealized first situation, being largest in the second. If the difference between the velocities of the CME leading edge and solar wind $[V_{\text{CME}} - V_{\text{SW}}]$ exceeds the fast-mode speed ahead the CME (as was the case in our event), then bow shock exists ahead of it with a speed practically equal to V_{CME} .

A model of the stationary solar wind is usually invoked to calculate V_{fast} . In a real situation, the CME formation is associated with the appearance of a large-scale fast-mode shock wave. Propagating up like a blast wave, it leaves behind an extended region, where V_{fast} is higher than the calculated value, so that $V_{\text{CME}} - V_{\text{SW}} < V_{\text{fast}}$ for some time. The CME expansion at this stage has the character of a flow and the bow shock is absent.

After that, a bow shock can appear even during the early CME expansion, but its role is insignificant, as long as the driving forces surpass the drag force. Only after the driving forces diminish relative to the drag force does the latter dominate the CME kinematics. Deceleration of both a freely propagating blast wave and bow shock ahead of a fast CME influenced by the aerodynamic drag complicates identification of the shock-wave regime. To assess the role of the drag at different distances, we will compare the observed velocity–distance plot with expectations for the bow-shock regime. We find the $V_{\text{CME}}(t)$ dependence required to calculate the bow-shock curves from the motion equation

$$m_{\text{CME}}(dV_{\text{CME}}/dt) = -\rho(V_{\text{CME}} - V_{\text{SW}})^2 S \equiv F_{\text{drag}}, \quad (1)$$

where m_{CME} is a constant effective mass of the CME and S is its cross-section. At a sufficient distance $S \propto r^2$. For simplicity we take V_{SW} at a reference distance

r_{ref} , neglecting its gradual variation in Equation (1). Due to conservation of the plasma flow in a stationary solar wind with a density ρ , $\rho S = \rho_{\text{ref}} S_{\text{ref}}$ is constant. The “ref” subscript corresponds to a distance r_{ref} or time t_{ref} . We transform Equation (1) to the form

$$dV_{\text{CME}}/dt = -C(V_{\text{CME}} - V_{\text{SW}})^2, \quad (2)$$

with $C = \rho_{\text{ref}} S_{\text{ref}} / m_{\text{CME}}$. The solution of Equation (2) is a function

$$V_{\text{CME}} = V_{\text{CME}}(t_{\text{ref}}) \left(1 + \kappa_{\text{ref}} \frac{t - t_{\text{ref}}}{\tau_{\text{ref}}}\right) \left(1 + \frac{t - t_{\text{ref}}}{\tau_{\text{ref}}}\right)^{-1} \quad (3)$$

with $\kappa_{\text{ref}} = V_{\text{SW}}/V_{\text{CME}}(t_{\text{ref}})$, $\tau_{\text{ref}} = [C(V_{\text{CME}}(t_{\text{ref}}) - V_{\text{SW}})]^{-1} = -[V_{\text{CME}}(t_{\text{ref}}) - V_{\text{SW}}]/a_{\text{ref}}$ being deceleration time scale, and $a_{\text{ref}} = (F_{\text{drag}}/M)_{t=t_{\text{ref}}} = [dV_{\text{CME}}/dt]_{t=t_{\text{ref}}}$ being the acceleration at a reference point. The characteristic deceleration time $[\tau_{\text{ref}}]$ is obtained by differentiation of Equation (3):

$$\tau_{\text{ref}} = (\kappa_{\text{ref}} - 1)V_{\text{CME}}(t_{\text{ref}})/[dV_{\text{CME}}/dt]_{t=t_{\text{ref}}}. \quad (4)$$

Figure 18 illustrates how the changing relation between the driving forces and drag force affects the CME deceleration. The black-solid line is a power-law fit of the observed velocity *vs.* distance dependence for the shock wave. The broken colored curves represent the trajectories $[V_{\text{CME}}(r)]$ calculated from Equations (3) and (4) for a constant CME mass. Each curve for the bow-shock regime is calculated by referring to the speeds of the shock and solar wind at three reference distances $r_{\text{ref}} = [6, 12, 18] R_{\odot}$. Drag is formally assumed to dominate at points r_{ref} , and the speeds of the shock front and CME are equal, $V_{\text{shock}} = V_{\text{CME}}$, *i.e.* the wave is bow shock. If the drag force surpassed the driving forces in the whole range of distances, then all four curves in Figure 18 would have coincided. In reality, the calculated curve approaches the experimental plot only at distances $r \geq r_{\text{ref}} \approx 15 R_{\odot}$, where aerodynamic drag can determine the CME deceleration.

6.2.3. Interplanetary Type II Event

We established consistency of a predicted Type II trajectory with observations up to a very low frequency of 250 kHz (Figure 12). This result reconciles the Type II emissions in the metric range with longer waves and addresses a long-standing discussion over their seemingly different origins (*e.g.* Cane and Erickson, 2005). Some other properties of the IP Type II become clearer.

A narrow-band Type II burst can only appear from a compact source in a narrow structure such as a coronal ray (Uralova and Uralov, 1994; Reiner *et al.*, 2003). Otherwise, a large shock front crossing a wide range of plasma densities produces a drifting continuum (Knock and Cairns, 2005). Coexisting signatures of two shocks in the Type II emission until 09:00 (Section 4.1) suggest a location of, at least, one of the sources at a flank of the shock wave. On the way to an observer, the emission crossing a dense heliospheric plasma sheet may be subjected to refraction, interference, and/or absorption. The IP Type II emission from a

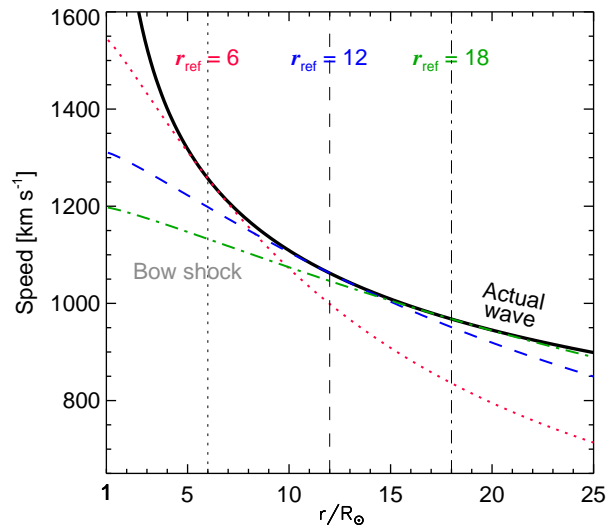


Figure 18. Comparison of the actual distance–speed wave evolution (same as in Figure 16c) with the plots expected for the bow-shock regime with different parameters (colored curves). The broken-vertical lines mark the reference distances r_{ref} , at which the speed and deceleration of the actual wave were taken to calculate corresponding plots for the bow-shock regime (denoted by the same colors and line styles).

moving compact source can fade and reappear, producing “blobs and bands” structures (Cane and Erickson, 2005). The structures of IP Type IIs observed from the vantage points of *Wind* and STEREO can therefore be different.

6.3. Particle Release

6.3.1. Type III Bursts and Particle Release

While remote-sensing methods for protons and heavier ions are limited by detection of γ -rays emitted in their interactions with dense material (*e.g.* Vilmer, MacKinnon, and Hurford, 2011), electrons can be used as their probable tracers. Their signatures extend from γ -ray bremsstrahlung continuum up to long radio waves. In the course of an eruptive flare, electrons and heavier particles are presumably injected from the reconnection site both down, into the flare loops, and up, into the forming flux rope. Electrons confined in a rising flux rope (which can also contain heavy particles) may produce a drifting Type IV burst. If reconnection between the flux rope and an open structure grants the trapped particles access to the interplanetary space, then a DH Type III burst produced by escaping electrons hints at a possible release of heavier particles.

Section 4.3 considered release of electrons trapped in the first flux rope after reconnection of its flank with a streamer or coronal hole producing Type III-1. Its onset corresponds to heights of the flux-rope’s top of $1.55 R_{\odot}$ and the reconnection site of $0.78 R_{\odot}$. Masson, Antiochos, and DeVore (2013) showed a possibility of SEP release in reconnection between a flux rope and coronal hole. In our event, the distance between AR 9742 and the southern coronal hole in

Figure 4 projected to this height was about $1 R_{\odot}$. The extra-radial divergence of magnetic field lines in a coronal hole makes its contact with a flux rope at this height possible. The left-handed flux rope with an axial field pointed the Northeast can reconnect with the southeasterly S-polarity coronal hole.

The appearance of a path to the interplanetary space could also release heavier particles trapped in the first flux rope before the Type III-1. Appropriate species supplied a rich seed population for acceleration by a trailing shock wave, which arrived in about five minutes, as Figure 17a shows. This probably occurred at one of the flanks of the flux rope and shock wave rather than at their noses.

The estimated height of the second flux-rope's top at the onset of Type III-2 is $2.1 R_{\odot}$. The height of the presumable reconnection site is $\approx 1.05 R_{\odot}$. Reconnection between the second flux rope expanding extra-radially and the coronal hole at this greater height is also probable. The starting frequency of Type III-2 expected at this height is 6.6 MHz (or 21 MHz for reconnection with the streamer); actually it was absent above 25 MHz and certainly present below 9 MHz, as Figure 10 in Section 4.3 shows. Its onset time, 05:27, is close to the SPR time of $05:29:00 \pm 3.7$ minutes estimated by Reames (2009a,b). However, the heliocentric distances of the particle release during Type III-1 and Type III-2 that we estimate for a CME flank are roughly about $2 R_{\odot}$ *vs.* $(3.6 \pm 0.5) R_{\odot}$ estimated by Reames (2009a,b) for the CME nose.

The absence of metric Type III bursts during DH Type III-1 and Type III-2 under the presence of accelerated electrons evidenced by flare emissions (Figure 10) indicates confinement of the magnetic configuration at that time. In contrast, the appearance of a dense metric Type III group associated with DH Type III-3 indicates that the configuration opened. Particles accelerated in the flare region gained direct access to the interplanetary space. Thus, the Type III-3 indicates a post-impulsive particle acceleration argued for in several studies (*e.g.* Chertok, 1995; Klein *et al.*, 1999, 2014). Although the related particle flux seems to be weaker than in the main flare, its contribution can be appreciable at moderate energies due to the long durations of post-eruption processes.

6.3.2. Particle Release in Other GLE Events

The preceding section confirms that DH Type III bursts (1–14 MHz) can trace release of heavy particles. To test how common this pattern is, we examined the GLEs analyzed by Reames (2009a), for which *Wind*/WAVES data are available. These are 13 out of 16 GLEs of Solar Cycle 23, excluding GLE55, GLE62, and GLE68, whose analysis was problematic. From one to four strong DH Type III bursts were observed in each event. The SPR time estimated by Reames (2009b) from the VDA analysis is typically close to one of these DH Type IIIs and never precedes their group. Coincidence is present in seven events, the interval between a Type III burst and the estimated SPR error band is within five minutes in four events, and the SPR time is considerably later than the Type IIIs in GLE58 (24 August 1998, ≈ 30 minutes) and GLE66 (29 October 2003, ≈ 15 minutes).

Following the traditional hypotheses, Reames (2009a,b) assumes that the shock wave starts to form when the CME exceeds the Alfvén speed ahead of it. The onset of a Type II burst is regarded as the onset of the shock formation.

The shock is assumed to strengthen afterwards. The SPR time is considered as a sign when the particle acceleration becomes efficient. However, the preceding section indicates that shock waves appear during the flare rise, being able to accelerate particles much earlier than traditionally assumed.

Reames (2009b) found for the 29 October 2003 event (GLE66) an SPR time of $20:55.6 \text{ ST} \pm 5.8 \text{ minutes}$, *i.e.* $21:03:56 \text{ UTC} \pm 5.8 \text{ minutes}$ for an observer on Earth. According to Balasubramaniam, Pevtsov, and Neidig (2007), a Moreton wave in this event started as early as 20:43 UTC and propagated with a speed of $1100 - 1200 \text{ km s}^{-1}$, which establishes its shock-wave regime. A Type II burst was observed at Culgoora (consistent with the Palehua spectrogram) starting at 430 MHz from 20:42 UTC, close to the Moreton wave onset. GLE66 started at 21:05 UTC (Gopalswamy *et al.*, 2012), and the onset of the $> 100 \text{ MeV}$ proton enhancement is detectable in the GOES-10 data at the same time. With a magnetic path length of $1.75 \pm 0.09 \text{ AU}$ (Reames, 2009b), the estimated SPR time seems to be too late.

Note that GLE66 occurred during the strongest Forbush decrease since the 1980s. It was caused by a huge magnetic cloud moving with a very high speed of 1900 km s^{-1} (Grechnev *et al.*, 2014a). Its rapid motion affected magnetic path lengths for different-energy particles, distorting the results of VDA.

Another exception is GLE58 on 24 August 1998. Reames (2009b) measured the SPR time for this event at $22:32.1 \text{ ST} \pm 4.6 \text{ minutes}$, *i.e.* $22:40:26 \text{ UTC} \pm 4.6 \text{ minutes}$. According to Vršnak *et al.* (2002), a Moreton wave started at 22:03 UTC with an initial speed of 946 km s^{-1} , decelerated like a blast wave, and covered 500 Mm. A Type II burst started at 22:02 UTC, close to the Moreton wave onset. The shock wave started early in this event. GLE58 started at 22:50 UTC (Gopalswamy *et al.*, 2012). A proton enhancement $> 100 \text{ MeV}$ is detectable at that time. With an estimated path length of $1.55 \pm 0.04 \text{ AU}$, the 100 MeV protons should have left the Sun by 22:29 UTC, well before the estimated SPR time, which is also challenging to understand.

There was no conspicuous anomaly in the Earth's environment during the GLE58 occurrence. A key can also be related to energy-dependent transport effects (drifts, diffusion, and others), whose importance is prompted by a moderately eastern position of the solar source region (E09 N35). Impressive transport issues were demonstrated by the 1 September 2014 solar event behind the east limb. The rise phase of a related proton enhancement was dominated during half a day by $> 100 \text{ MeV}$ protons, whereas their expected flux should be suppressed.

Most likely, the uncertainties of the VDA results obtained by Reames (2009b) for the 13 GLEs of Solar Cycle 23 were underestimated because of transport effects not considered (Laitinen *et al.*, 2015 analyzed some corrections in the VDA). Presumably realistic SPR times in these events were close to the DH Type III bursts, suggesting concurrent release of heavy particles and electrons, probably accelerated by flare processes. A detailed analysis of the 2 May 1998 (GLE56) and 2 November 2003 (GLE67) events by Kocharov *et al.* (2017) has led to a similar scenario.

However, the VDA has not revealed an expected earlier population accelerated by shock waves, which should appear during the flare impulsive phase. The shock-accelerated population should exist, dominating at low energies. Possibly,

the seed population is supplied by a preceding eruption, as in our event. In this case, ions released from a flux rope should inherit the properties of a flare region such as a high iron ionization state (*cf.* Desai *et al.*, 2006), but this is not always the case (see Section 2). Possibly, material of quiet coronal structures swept up by the top of an expanding flux rope can be implicated. These circumstances call for rethinking the conditions of particle acceleration by shock waves and the signatures of these particles.

Note that magnetic confinement of protons and heavier ions is not as tight as that of electrons. Having much larger gyroradii, heavy particles can escape more easily than electrons. Therefore, DH Type III bursts hint at the most effective release of heavy particles, while their escape is possible at different times.

The flux-rope-mediated escape of accelerated protons and electrons is different. The mean free path of a fast ion with a mass $[m_i]$, charge $[e_i]$, and an initial velocity $[v_0]$ in plasma with a number density $[n]$ is $\lambda_i = m_i m_e v_0^4 / (16\pi e_i^2 e_e^2 \Lambda n)$, where $\Lambda \approx 10$ is Coulomb logarithm, $[e_e]$ and $[m_e]$ are the electron charge and mass; $\tau_{\text{coll}} \approx \lambda_i / v_0$. The lifetime of relativistic electrons with an energy E_e is $\tau_{\text{life}(e)} \approx 2.6 \times 10^9 E_e / n$. For example, the lifetime of 100 MeV protons exceeds the lifetime of 0.5 MeV electrons in the same plasma by two orders of magnitude. Thus, the electron-to-proton ratio escaping from a flux rope with an initial $n > 10^{10} \text{ cm}^{-3}$ may be much less than for their direct escape from the flare site.

7. Summary

Combining observations of the 26 December 2001 event in various spectral ranges, we reconstructed its scenario and histories of the CME and shock wave. This solar event consisted of the following episodes. i) The first flux-rope's eruption started around 04:30. ii) The second, largest eruption around 05:04 produced the first shock wave and the main CME. iii) The third, jet-like eruption around 05:09 produced the second shock wave. Each wave was most likely impulsively excited by an abruptly erupting flux rope, rapidly steepened into a shock due to a steep falloff of the fast-mode speed outward from the eruption region, and initially resembled a blast wave. Both waves ultimately merged around the radial direction into a single stronger shock wave. Being followed by a fast CME body, it should eventually change to the bow-shock regime.

- i) The shock wave within the LASCO field of view was in an intermediate regime between the two extremities of blast wave and bow shock. The wave kinematics was controlled by the trailing CME, whose mass grew at the first stage because of the swept-up plasma. This factor, missed in many studies, determined strong deceleration of the wave at this stage, different from the bow-shock regime, which becomes possible at distances $> 15 R_{\odot}$.

The Type II emission in this event was traced from meters up to ≈ 250 kHz. Two shock waves coexisted at moderate distances from the Sun. This rules out the bow-shock regime at this stage and indicates location of, at least, one of the radio sources at a flank of the shock. Correspondence of a calculated

trajectory to the overall observed evolution of the Type II emissions in the whole frequency range demonstrates their common origin.

The shock excitation scenario described here was the only one in eruptive flares that we studied so far with a GOES importance from B to X class. Neither did we observe a different overall history of the shock wave ahead of a fast CME.

- ii) Shock waves appear during the flare rise, being able to accelerate particles much earlier than usually assumed. A delayed particle release time suggests instead their acceleration during the flare and accumulation in the flux-rope's magnetic trap until the access to the interplanetary space appears, which is possible in reconnection of the flux rope with an open structure. The rate of particle escape from the trap (*i.e.* their flux) can considerably exceed the rate of their injection into the trap during the flare. This transport scenario can account for the contrast between the strong proton flux and a microwave burst, which was not extreme on 26 December 2001.

The flux-rope-mediated transport scenario is supported by the closeness of the estimated particle release to the DH Type III bursts in most GLE events of Solar Cycle 23. This scenario can also supply the seed population for acceleration by a trailing shock wave. In this case, particles are most likely released at the flank of an expanding flux rope and shock wave. This results in considerably lesser heights of particle release than usually assumed.

- iii) The first eruption stretched closed structures above the active region, facilitating escape of flare-accelerated particles and lift-off of the main CME. Having not spent a part of its energy to overcome the magnetic tension of closed structures and to sweep up plasma ahead, the main CME could reach a higher speed and drive a stronger shock. Thus, the preceding eruption could have amplified the outcome of both flare-accelerated and shock-accelerated protons. Another factor was excitation of two shock waves, eventually merging in a stronger shock. Both of these factors can amplify solar particle events.

Acknowledgments We thank B.I. Lubyshev, N.V. Nitta, I.M. Chertok, and H.V. Cane for discussions and assistance, and Y. Kubo for preparing the HiRAS spectra for us. We are indebted to an anonymous reviewer for valuable remarks. We thank the instrument teams of EIT, LASCO, and MDI on SOHO (ESA and NASA), *Wind*/WAVES, GOES, TRACE, and MLSO operated by NCAR/HAO; NICT (Japan); USAF RSTN Network; and the CME Catalog at the CDAW Data Center (NASA and Catholic University of America) for the data used in this study. The study was supported by the Russian State Contracts No. II.16.3.2 and No. II.16.1.6. A. Kochanov was supported by the Russian Foundation of Basic Research under grants 15-02-03717 and 15-02-01089. V. Kiselev was supported by the Marie Curie PIRSES-GA-2011-295272 RadioSun project.

Disclosure of Potential Conflicts of Interest

The authors claim that they have no conflicts of interest.

References

Afanasyev, A.N., Uralov, A.M., Grechnev, V.V.: 2013, *Astron. Rep.*, **57**, 594. DOI

- Akinian, S.T., Alibegov, M.M., Kozlovski, V.D., Chertok, I.M.: 1978, *Geomagn. Aeron.*, **18**, 410.
- Aschwanden, M.J.: 2012, *Space Sci. Rev.* **173**, 3. DOI
- Balasubramaniam, K.S., Pevtsov, A.A., Neidig, D.F.: 2007, *Astrophys. J.* **658**, 1372. DOI
- Belov, A.V., Eroshenko, E.A., Kryakunova, O.N., Kurt, V.G., Yanke, V.G.: 2010, *Geomagnetism and Aeronomy* **50**, 21. DOI
- Bougeret, J.-L., Kaiser, M.L., Kellogg, P.J., Manning, R., Goetz, K., Monson, S.J., Monge, N., Friel, L., Meetre, C.A., Perche, C., Sitruk, L., Hoang, S.: 1995, *Space Sci. Rev.* **71**, 231. DOI
- Brueckner, G.E., Howard, R.A., Koomen, M.J., Korendyke, C.M., Michels, D.J., Moses, J.D., Socker, D.G., Dere, K.P., Lamy, P.L., Llebaria, A., *et al.*: 1995, *Solar Phys.* **162**, 357. DOI
- Cane, H.V., Erickson, W.C.: 2005, *Astrophys. J.* **623**, 1180. DOI
- Castelli, J.P., Barron, W.R.: 1977, *J. Geophys. Res.* **82**, 1275. DOI
- Chertok, I.M.: 1995, in N. Iucci and E. Lamanna (eds.) *24th International Cosmic Ray Conference*. International Union of Pure and Applied Physics. Rome, Italy, **4**, 78.
- Chupp, E.L., Ryan, J.M.: 2009, *Res. Astron. Astrophys.* **9**, 11. DOI
- Ciaravella, A., Raymond, J.C., Kahler, S.W.: 2006, *Astrophys. J.* **652**, 774. DOI
- Cliwer, E.W.: 2006, *Astrophys. J.* **639**, 1206. DOI
- Croom, D.L.: 1971, *Solar Phys.* **19**, 171. DOI
- Delaboudinière, J.-P., Artzner, G.E., Brunaud, J., Gabriel, A.H., Hochedez, J.F., Millier, F., Song, X.Y., Au, B., Dere, K.P., Howard, R.A., *et al.*: 1995, *Solar Phys.* **162**, 291. DOI
- Desai, M.I., Mason, G.M., Gold, R.E., Krimigis, S.M., Cohen, C.M.S., Mewaldt, R.A., Mazur, J.E., Dwyer, J.R.: 2006, *Astrophys. J.* **649**, 470. DOI
- Dierckxens, M., Tziotziou, K., Dalla, S., Patsou, I., Marsh, M.S., Crosby, N.B., Malandraki, O., Tsiropoula, G.: 2015, *Solar Phys.* **290**, 841. DOI
- Filippov, B., Golub, L., Koutchmy, S.: 2009, *Solar Phys.* **254**, 259. DOI
- Geier, S., Barbier, L.M., Binns, W.R., Christian, E.R., Cummings, J.R., de Nolfo, S.M., Israel, M.H., Link, J.T., Mewaldt, R.A., Mitchell, J.W., *et al.*: 2003, in: T. Kajita, Y. Asaoka, A. Kawachi, Y. Matsubara, and M. Sasaki (eds.) *28th International Cosmic Ray Conference*. Universal Academy Press, Tokyo, Japan. **6**, 3261.
- Gopalswamy, N., Mäkelä, P., Akiyama, S., Yashiro, S., Xie, H., Thakur, N., Kahler, S.W.: 2015, *Astrophys. J.* **806**, 8. DOI
- Gopalswamy, N., Xie, H., Yashiro, S., Akiyama, S., Mäkelä, P., Usoskin, I.G.: 2012, *Space Sci. Rev.* **171**, 23. DOI
- Grechnev, V.V.: 2003, *Solar Phys.* **213**, 103. DOI
- Grechnev, V.V., Kochanov, A.A.: 2016, *Solar Phys.* **291**, (Article I). DOI
- Grechnev, V.V., Lesovoi, S.V., Smolkov, G.Y., Krissinel, B.B., Zandanov, V.G., Altyntsev, A.T., Kardapolova, N.N., Sergeev, R.Y., Uralov, A.M., Maksimov, V.P., Lubyshev, B.I.: 2003, *Solar Phys.* **216**, 239. DOI
- Grechnev, V.V., Uralov, A.M., Zandanov, V.G., Rudenko, G.V., Borovik, V.N., Grigorieva, I.Y., Slemzin, V.A., Bogachev, S.A., Kuzin, S.V., Zhitnik, I., Pertsov, A.A., Shibasaki, K., Livshits, M.A.: 2006, *Publ. Astron. Soc. Japan* **58**, 55. DOI
- Grechnev, V.V., Kurt, V.G., Chertok, I.M., Uralov, A.M., Nakajima, H., Altyntsev, A.T., Belov, A.V., Yushkov, B.Y., Kuznetsov, S.N., Kashapova, L.K., Meshalkina, N.S., Prestage, N.P.: 2008a, *Solar Phys.* **252**, 149. DOI
- Grechnev, V.V., Uralov, A.M., Slemzin, V.A., Chertok, I.M., Kuzmenko, I.V., Shibasaki, K.: 2008b, *Solar Phys.* **253**, 263. DOI
- Grechnev, V.V., Uralov, A.M., Chertok, I.M., Kuzmenko, I.V., Afanasyev, A.N., Meshalkina, N.S., Kalashnikov, S.S., Kubo, Y.: 2011, *Solar Phys.* **273**, 433. DOI
- Grechnev, V.V., Kiselev, V.I., Uralov, A.M., Meshalkina, N.S., Kochanov, A.A.: 2013a, *Publ. Astron. Soc. Japan* **65**, SP1, S9. DOI
- Grechnev, V.V., Meshalkina, N.S., Chertok, I.M., Kiselev, V.I.: 2013b, *Publ. Astron. Soc. Japan* **65**, SP1, S4. DOI
- Grechnev, V.V., Uralov, A.M., Chertok, I.M., Belov, A.V., Filippov, B.P., Slemzin, V.A., Jackson, B.V.: 2014a, *Solar Phys.* **289**, 4653. DOI
- Grechnev, V.V., Uralov, A.M., Chertok, I.M., Slemzin, V.A., Filippov, B.P., Egorov, Ya.I., Fainshtein, V.G., Afanasyev, A.N., Prestage, N., Temmer, M.: 2014b, *Solar Phys.* **289**, 1279. DOI
- Grechnev, V.V., Kiselev, V.I., Meshalkina, N.S., Chertok, I.M.: 2015a, *Solar Phys.* **290**, 2827. DOI

- Grechnev, V.V., Uralov, A.M., Kuzmenko, I.V., Kochanov, A.A., Chertok, I.M., Kalashnikov, S.S.: 2015b, *Solar Phys.* **290**, 129. DOI
- Grechnev, V.V., Uralov, A.M., Kochanov, A.A., Kuzmenko, I.V., Prosovetsky, D.V., Egorov, Y.I., Fainshtein, V.G., Kashapova, L.K.: 2016, *Solar Phys.* **291**, 1173. DOI
- Grechnev, V.V., Uralov, A.M., Kiselev, V.I., Kochanov, A.A.: 2017, *Solar Phys.* **292**: 3. (Article II). DOI
- Handy, B.N., Acton, L.W., Kankelborg, C.C., Wolfson, C.J., Akin, D.J., Bruner, M.E., Carvalho, R., Catura, R.C., Chevalier, R., Duncan, D.W., *et al.*: 1999, *Solar Phys.* **187**, 229. DOI
- Kahler, S.W.: 1982, *J. Geophys. Res.* **87**, 3439. DOI
- Kallenrode, M.-B.: 2003, *J. Phys. G Nuclear Phys.* **29**, 965. DOI
- Klein, K.-L., Trottet, G.: 2001, *Space Sci. Rev.* **95**, 215. DOI
- Klein, K.-L., Mouradian, Z.: 2002, *Astron. Astrophys.* **381**, 683. DOI
- Klein, K.-L., Chupp, E.L., Trottet, G., Magun, A., Dunphy, P.P., Rieger, E., Urpo, S.: 1999, *Astron. Astrophys.* **348**, 271.
- Klein, K.-L., Masson, S., Bouratzis, C., Grechnev, V., Hillaris, A., Preka-Papadema, P.: 2014, *Astron. Astrophys.* **572**, AA4. DOI
- Kocharov, L., Pohjolainen, S., Mishev, A., Reiner, M.J., Lee, J., Laitinen, T., Didkovsky, L.V., Pizzo, V.J., Kim, R., Klassen, A., Karlicky, M., Cho, K.-S., Gary, D.E., Usoskin, I., Valtonen, E., Vainio, R.: 2017, *Astrophys. J.* **839**, 79. DOI
- Knock, S.A., Cairns, I.H.: 2005, *J. Geophys. Res. A* **110**, A01101. DOI
- Kwon, R.-Y., Zhang, J., Olmedo, O.: 2014, *Astrophys. J.* **794**, 148. DOI
- Kwon, R.-Y., Zhang, J., Vourlidas, A.: 2015, *Astrophys. J. Lett.* **799**, L29. DOI
- Laitinen, T., Huttunen-Heikinmaa, K., Valtonen, E., Dalla, S.: 2015, *Astrophys. J.* **806**, 114. DOI
- Lario, D., Aran, A., Decker, R.B.: 2009, *Solar Phys.* **260**, 407. DOI
- Mann, G., Klassen, A., Aurass, H., Classen, H.-T.: 2003, *Astron. Astrophys.* **400**, 329. DOI
- Masson, S., Antiochos, S.K., and DeVore, C.R.: 2013, *Astrophys. J.* **771**, 82. DOI
- Masson, S., Pariat, E., Aulanier, G., Schrijver, C.J.: 2009, *Astrophys. J.* **700**, 559. DOI
- McLean, D.J.: 1973, *Proc. Astron. Soc. Australia* **2**, 222.
- Melnikov, V.F., Podstrigach, T.S., Dajbog, E.I., Stolpovskij, V.G.: 1991, *Cosmic Res.* **29**, 87.
- Meshalkina, N.S., Uralov, A.M., Grechnev, V.V., Altyntsev, A.T., Kashapova, L.K.: 2009, *Publ. Astron. Soc. Japan* **61**, 791. DOI
- Mewaldt, R.A., Looper, M.D., Cohen, C.M.S., Haggerty, D.K., Labrador, A.W., Leske, R.A., Mason, G.M., Mazur, J.E., von Rosenvinge, T.T.: 2012, *Space Sci. Rev.* **171**, 97. DOI
- Miklenic, C.H., Veronig, A.M., Vršnak, B.: 2009, *Astron. Astrophys.* **499**, 893. DOI
- Miroshnichenko, L.I., Vashenyuk, E.V., Pérez-Peraza, J.A.: 2013, *Geomag. Aeron.* **53**, 541. DOI
- Nakajima, H., Nishio, M., Enome, S., Shibasaki, K., Takano, T., Hanaoka, Y., Torii, C., Sekiguchi, H. *et al.*: 1994, *Proc. IEEE* **82**, 705. DOI
- Nakajima, H., Sekiguchi, H., Sawa, M., Kai, K., Kawashima, S.: 1985, *Publ. Astron. Soc. Japan* **37**, 163.
- Neupert W.M.: 1968, *Astrophys. J. Lett.* **153**, L59. DOI
- Newkirk, G. Jr.: 1961, *Astrophys. J.* **133**, 983. DOI
- Nitta, N.V., Liu, Y., DeRosa, M.L., Nightingale, R.W.: 2012, *Space Sci. Rev.* **171**, 61. DOI
- Qiu J., Hu Q., Howard T., Yurchyshyn V.: 2007, *Astrophys. J.* **659**, 758. DOI
- Reames, D.V.: 2009a, *Astrophys. J.* **693**, 812. DOI
- Reames, D.V.: 2009b, *Astrophys. J.* **706**, 844. DOI
- Reames, D.V.: 2013, *Space Sci. Rev.* **175**, 53. DOI
- Reiner, M.J., Vourlidas, A., St. Cyr, O.C., Burkepile, J.T., Howard, R.A., Kaiser, M.L., Prestage, N.P., Bougeret, J.-L.: 2003, *Astrophys. J.* **590**, 533. DOI
- Rouillard, A.P., Sheeley, N.R., Tylka, A., Vourlidas, A., Ng, C.K., Rakowski, C., Cohen, C.M.S., Mewaldt, R.A., Mason, G.M., Reames, D., Savani, N.P., St. Cyr, O.C., Szabo, A.: 2012, *Astrophys. J.* **752**, 44. DOI
- Saito, K.: 1970, *Ann. Tokyo Astr. Obs.* **12**, 53.
- Saito, K., Poland, A.I., and Munro, R.H.: 1977, *Solar Phys.* **55**, 121. DOI
- Scherrer, P.H., Bogart, R.S., Bush, R.I., Hoeksema, J.T., Kosovichev, A.G., Schou, J., Rosenberg, W., Springer, L., Tarbell, T.D., Title, A., *et al.*: 1995, *Solar Phys.* **162**, 129. DOI

-
- Sheeley, N.R., Wang, Y.-M., Hawley, S.H., Brueckner, G.E., Dere, K.P., Howard, R.A., Koomen, M.J., Korendyke, C.M., Michels, D.J., Paswaters, S.E., *et al.*: 1997, *Astrophys. J.* **484**, 472.
- Smolkov, G.I., Piskolkors, A.A., Treskov, T.A., Krissinel, B.B., Putilov, V.A.: 1986, *Astrophys. Spa. Sci.* **119**, 1. DOI
- Temmer, M., Veronig, A.M., Vršnak, B., Rybák, J., Gömöry, P., Stoiser, S., Maričić, D.: 2008, *Astrophys. J.* **673**, 95. DOI
- Temmer, M., Veronig, A., Kontar, E., Krucker, S., Vršnak, B.: 2010, *Astrophys. J.* **712**, 1410. DOI
- Trottet, G., Samwel, S., Klein, K.-L., Dudok de Wit, T., Miteva, R.: 2015, *Solar Phys.* **290**, 819. DOI
- Tylka, A.J., Lee, M.A.: 2006, *Astrophys. J.* **646**, 1319. DOI
- Tylka, A.J., Cohen, C.M.S., Dietrich, W.F., Lee, M.A., MacLennan, C.G., Mewaldt, R.A., Ng, C.K., Reames, D.V.: 2005, *Astrophys. J.* **625**, 474. DOI
- Tylka, A.J., Malandraki, O.E., Dorrian, G., Ko, Y.-K., Marsden, R.G., Ng, C.K., Tranquille, C.: 2013, *Solar Phys.* **285**, 251. DOI
- Uralov, A.M., Grechnev, V.V., Rudenko, G.V., Myshyakov, I.I., Chertok, I.M., Filippov, B.P., Slemzin, V.A.: 2014, *Solar Phys.* **289**, 3747. DOI
- Uralova, S.V., Uralov, A.M.: 1994, *Solar Phys.* **152**, 457. DOI
- Vilmer, N., MacKinnon, A.L., Hurford, G.J.: 2011, *Space Sci. Rev.* **159**, 167. DOI
- Vršnak, B., Cliver, E.W.: 2008, *Solar Phys.* **253**, 215. DOI
- Vršnak, B., Warmuth, A., Brajša, R., Hanslmeier, A.: 2002, *Astron. Astrophys.* **394**, 299. DOI
- Yashiro, S., Gopalswamy, N., Michalek, G., St. Cyr, O.C., Plunkett, S.P., Rich, N.B., Howard, R.A.: 2004, *J. Geophys. Res.* **109**, A07105. DOI
- Zhang, J., Dere, K.P., Howard, R.A., Kundu, M.R., White, S.M.: 2001, *Astrophys. J.* **559**, 452. DOI